





RESEARCH ARTICLE | APRIL 14 2023

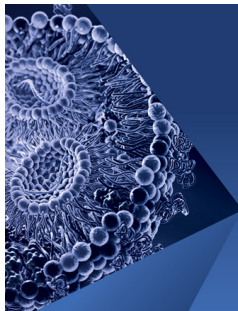
## Direct numerical simulations of hypersonic boundary layer transition over a hypersonic transition research vehicle model lifting body at different angles of attack

Men Hongyuan (门弘远) ; Li Xinliang (李新亮) ; Liu Hongwei (刘洪伟)  



*Physics of Fluids* 35, 044111 (2023)

<https://doi.org/10.1063/5.0146651>



## Physics of Fluids

Special Topic:

Flow and Lipid Nanoparticles

Guest Editors: Richard Braatz and Mona Kanso

[Submit Today!](#)

# Direct numerical simulations of hypersonic boundary layer transition over a hypersonic transition research vehicle model lifting body at different angles of attack

Cite as: Phys. Fluids **35**, 044111 (2023); doi: 10.1063/5.0146651

Submitted: 15 February 2023 · Accepted: 31 March 2023 ·

Published Online: 14 April 2023



View Online



Export Citation



CrossMark

Hongyuan Men (门弘远),<sup>1,2</sup> Xinliang Li (李新亮),<sup>1,2</sup> and Hongwei Liu (刘洪伟)<sup>1,a)</sup>

## AFFILIATIONS

<sup>1</sup>LHD, Institute of Mechanics, Chinese Academy of Sciences, Beijing 100190, China

<sup>2</sup>School of Engineering Science, University of Chinese Academy of Sciences, Beijing 100049, China

<sup>a)</sup> Author to whom correspondence should be addressed: [hliu@imech.ac.cn](mailto:hliu@imech.ac.cn)

## ABSTRACT

This paper performs direct numerical simulations of hypersonic boundary layer transition over a Hypersonic Transition Research Vehicle (HyTRV) model lifting body designed by the China Aerodynamic Research and Development Center. Transitions are simulated at four angles of attack: 0°, 3°, 5°, and 7°. The free-stream Mach number is 6, and the unit Reynolds number is  $10^7 \text{ m}^{-1}$ . Four distinct transitional regions are identified: the shoulder cross-flow and vortex region and the shoulder vortex region on the leeward side, the windward vortex region and the windward cross-flow region on the windward side. As the angle of attack increases, the transition locations on the leeward side generally move forward and the transition ranges expand, while the transition locations generally move backward and the transition ranges decrease on the windward side. Moreover, the shoulder vortex region moves toward the centerline of the leeward side. At large angles of attack (5° and 7°), the streamwise vortex on the shoulder cross-flow and vortex region will enable the transition region to be divided into the cross-flow instability region on both sides and the streamwise vortex instability region in the middle. In addition, the streamwise vortex also leads to a significant increase in cross-flow instability in their upper region, which can generate a new streamwise vortex instability region between the two transition regions on the leeward side. Furthermore, since the decrease in the intensity and the range for the cross-flow on the windward side, the windward cross-flow region tends to become narrow and ultimately disappears.

Published under an exclusive license by AIP Publishing. <https://doi.org/10.1063/5.0146651>

## I. INTRODUCTION

The transition problem is one of the few fundamental subject problems left over from classical mechanics.<sup>1–3</sup> The transition from laminar to turbulent flow significantly alters factors such as skin friction, noise, heat transfer, and mixing.<sup>4</sup> Typically, the skin friction and heat flow in turbulent flow are 3–5 times greater than that of laminar flow.<sup>5</sup> This difference will be significantly enhanced at hypersonic speed and will greatly impact the aerodynamic performance and thermal protection system of hypersonic vehicles.<sup>6,7</sup>

Currently, numerous research efforts have been directed toward understanding hypersonic boundary layer transition.<sup>8–11</sup> Nevertheless, the underlying mechanisms of induced boundary layer transition remain poorly understood. As a result, no model or semi-empirical formula can accurately predict hypersonic boundary layer transition under a broad range of flight conditions.<sup>12,13</sup> This limitation greatly

hinders the development of high-speed missiles, hypersonic reentry vehicles, hypersonic cruise vehicles, and other vehicles.

Initially, the research on hypersonic boundary layer transition mainly focused on simple configurations, such as flat plates and concave walls.<sup>14–16</sup> Kornilov<sup>17</sup> studied the boundary layer transition over a smooth plate at zero angle of attack in the range of Mach = 2–6 and found an approximate method with low error and a wide range of applicability for measuring the end of the transition region. Fedorov<sup>18</sup> has summarized research on various aspects of high-speed boundary layer transition, particularly emphasizing the differences between hypersonic, subsonic, and moderate-supersonic transitions over a flat plate at zero angle of attack. Lu *et al.*<sup>19</sup> employed Nano-tracer Planar Laser Scattering (NPLS) and Temperature-Sensitive Paints (TSP) methods to investigate the instantaneous fine structure of the boundary layer over a 45° swept slab in a hypersonic low-noise wind tunnel

at a Mach number of 6. Chen *et al.*<sup>20</sup> studied the hypersonic boundary layer transition on a concave wall induced by unsteady low-frequency blowing and suction and found that diamond-shaped and  $\Lambda$ -shaped structures induced by Görtler instability waves or first-mode instability waves are highly susceptible to high-frequency secondary instabilities, and further carried out two kinds of instability waves energy analysis. Chen *et al.*<sup>21</sup> performed a direct numerical simulation on the boundary layer of a swept-wing with a sweep angle of  $45^\circ$  and analyzed in depth the instability mechanism of stationary cross-flow vortices breakdown of the high-speed cross-flow transition to full turbulence.

As the field of hypersonic boundary layer transition research continues to develop, the focus of research has been changed to other boundary layers with more complex shapes. Among these, the cone, which serves as the head of many hypersonic vehicles, has recently attracted much attention.<sup>22,23</sup> Stetson and Kimmel<sup>24</sup> performed experiments on the stability of the hypersonic boundary layer over a  $7^\circ$  half-cone-angle and  $0^\circ$  angle of attack blunt cone and measured the wave spectrum at various positions. Su *et al.*<sup>25</sup> developed a new method that accounted for both the attenuation and amplification of disturbance waves and applied this method to study a Mach 6 blunt cone. Li *et al.*<sup>26</sup> conducted a direct numerical simulation of the hypersonic boundary layer transition over a  $5^\circ$  half-cone-angle blunt cone. They obtained the non-monotonic transition line on the cone and analyzed the mechanism of delayed transition. Wang *et al.*<sup>27</sup> investigated the effects of wall temperature on hypersonic boundary layer transition over an inclined blunt cone with two wall temperatures and studied the breakdown process of leeward streamwise vortices and crossflow vortices.

To meet the demands of high-speed, high-altitude, and long-distance cruising for hypersonic vehicles, the design of lifting bodies with high lift-to-drag ratios and strong maneuverability has become a recent research focus.<sup>28–30</sup> The prediction, mechanism, and control methods of hypersonic boundary layer transition for lifting bodies have also become essential design considerations for these vehicles.<sup>31</sup> Despite the lifting body having a high lift-to-drag ratio, it has poor stability, particularly lateral stability. Gao *et al.*<sup>32</sup> conducted experiments on two types of lifting bodies in wind tunnels with different Mach and Reynolds numbers and discovered that lifting bodies will have self-excited vibration caused by the asymmetric transition at the nose at low angles of attack. They also found that there are three distinct scales present in hypersonic lateral separation or transition flow. Wartemann *et al.*<sup>33</sup> conducted hypersonic reentry flight experiments on a sharp-edged lifting body and a blunt-edged lifting body and found that the sharp-edged lifting body, with its advanced design and lower production cost, had a higher lift-to-drag ratio and lowered thermal load.

The HyTRV model is a lifting body model with typical hypersonic vehicle characteristics. By HyTRV, we mean a Hypersonic Transition Research Vehicle, which was designed by the China Aerodynamic Research and Development Center.<sup>34</sup> The model's geometry profile is completely generated by analytical functions, and its flow region exhibits several instabilities. Therefore, the HyTRV model is an ideal candidate for the study of hypersonic boundary layer transition. Chen *et al.*<sup>35</sup> conducted a parametric study on the typical flow characteristics and boundary layer instability characteristics of the HyTRV model at different angles of attack through a one-dimensional stability analysis. They also provided suggestions for future research based on the types of instability found on the HyTRV model at different angles of attack. Qi *et al.*<sup>36</sup> conducted a direct

numerical simulation of the hypersonic boundary layer transition over a HyTRV model at  $0^\circ$  angle of attack under typical wind tunnel conditions and analyzed the instability mode of each region. Chen *et al.*<sup>37</sup> performed numerical simulations and multi-dimensional linear stability analyses for the HyTRV model at  $2^\circ$  angle of attack at the same flow conditions as Qi *et al.*<sup>36</sup> They also carried out a study on the dominant transition mechanism in some selected regions of interest.

Despite the progress mentioned above made in research on the HyTRV model, there are still some problems that remain. First, both Chen *et al.*<sup>35</sup> and Chen *et al.*<sup>37</sup> found that the flow field distribution and structure around the HyTRV model at a laminar state can be greatly affected by the changes in the angle of attack, which results in the transition mechanism over the HyTRV model more complex. However, previous studies on the hypersonic boundary layer transition over the HyTRV model have only been conducted at small angles of attack of  $0^\circ$  or  $2^\circ$ . Thus, further research on it at larger angles of attack is needed. Second, previous studies on the transition of the hypersonic boundary layer have only been conducted on a single angle of attack for the HyTRV model. There is a lack of comparative analysis of the transition region and transition mechanism between the HyTRV models at different angles of attack.

In this paper, direct numerical simulations (DNS) of the hypersonic boundary layer transition over a HyTRV model lifting body are conducted at different angles of attack, under the same flow conditions as Qi *et al.*,<sup>36</sup> in order to conduct a comparative analysis with previous studies. A total of  $1.4 \times 10^9$  grids are used in simulations. The angles of attack are  $0^\circ$ ,  $3^\circ$ ,  $5^\circ$ , and  $7^\circ$ . According to the comparative analysis with the flow field data of the HyTRV model at different angles of attack, the development characteristics of the location, range and transition mechanism for each hypersonic boundary layer transition region are summarized.

The paper is organized as follows. The numerical settings are introduced in Sec. II. The results of numerical simulations and corresponding analysis are presented in Sec. III. A summary and conclusion are offered in Sec. IV.

## II. NUMERICAL SETTINGS

### A. The HyTRV model

The specific information of the HyTRV model can be obtained from the research of Liu *et al.*<sup>34</sup> As shown in Figs. 1 and 2, the HyTRV model has an overall length of 1600 mm and its head is a 2:1:1 ellipsoid. The cross section of the HyTRV model is composed of a windward side located below and a leeward side located above. The windward side is a 4:1 elliptic curve, while the leeward side is composed of a Class/Shape Function Transformation (CST) curve and a 4:1 elliptic curve.

The generating function for the leeward curve (CST) in the tail cross section is

$$\begin{aligned} Y &= \cos \theta W_t, \quad \theta \in [0, \pi], \\ Z &= \alpha Z_C + (1 - \alpha) Z_E. \end{aligned} \quad (1)$$

The calculation function of  $Z_C$  is

$$\begin{aligned} Z_C &= \zeta H_I, \\ \zeta &= 2^8 \cdot \eta^4 \cdot (1 - \eta)^4, \\ \eta &= \frac{1}{2} \cos \theta + \frac{1}{2}, \quad \theta \in [0, \pi]. \end{aligned} \quad (2)$$

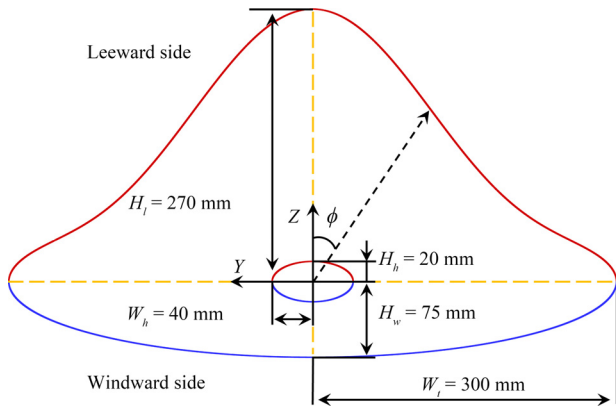


FIG. 1. Cross-sectional for the head and tail of the HyTRV model. The blue line represents the windward side, and the red line represents the leeward side, consistent with the size of the model of the previous study.<sup>36,37</sup>

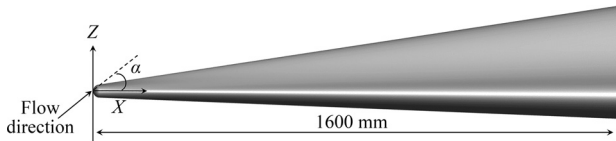


FIG. 2. Side view of the HyTRV model.  $\alpha$  is the angle of attack of the model.

The calculation functions of  $Z_E$  and  $\alpha$  are

$$\begin{aligned} Z_E &= \sin \theta H_l, \\ \alpha &= 1 - \frac{H_w}{H_l}, \end{aligned} \quad (3)$$

where  $H_w$  is the height of the windward side,  $H_l$  is the height of the leeward side, and  $W_t = 4H_w$  is half the width of the cross section of the tail.  $\theta$  is a parameter ranging from 0 and  $\pi$ .

### B. Flow conditions

The typical hypersonic wind tunnel flow conditions are used. The gas species considered is air. The specific flow parameters are shown in Table I, where  $Ma_\infty$  is the free-stream Mach number,  $Re_\infty$  is the unit Reynolds number,  $\rho_\infty$  is the free-stream density,  $P_\infty$  is the static pressure,  $T_\infty$  is the static temperature,  $T_w$  is the wall temperature,  $T_0$  is the total temperature, and  $h_0$  is the free-stream stagnation enthalpy. Four angles of attack are used:  $0^\circ$ ,  $3^\circ$ ,  $5^\circ$ , and  $7^\circ$ .

### C. Numerical simulations

The numerical simulation strategy consists of two steps: laminar simulation and transition simulation. Under the flow conditions

TABLE I. Flow parameters.

$Ma_\infty$	$Re_\infty$ ( $m^{-1}$ )	$\rho_\infty$ ( $kg/m^3$ )	$P_\infty$ (Pa)	$T_\infty$ (K)	$T_w$ (K)	$T_0$ (K)	$h_0$ (J/kg)
6	$10^7$	0.051	1147	79	300	648	$6.5 \times 10^5$

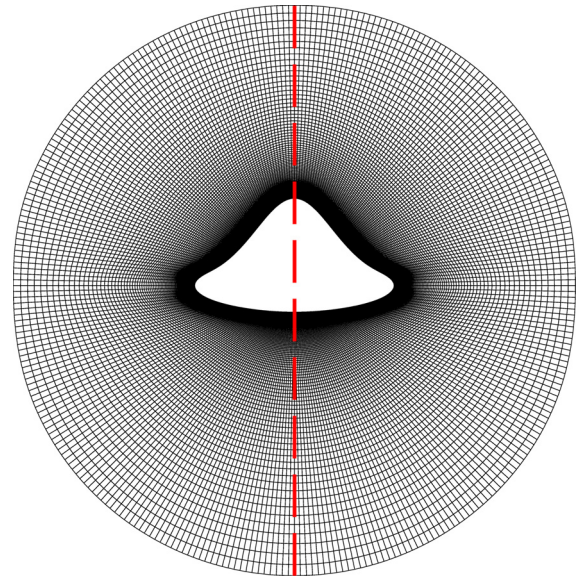


FIG. 3. Cross section grid distribution in the laminar simulation ( $X = 1500$  mm). The left side of the red dotted line is the grid used in the actual laminar simulation. The right side of the red dotted line is the mirror grid on its left side.

currently used, the pressure of the gas is low enough and the temperature of the gas is not too high (the total temperature is 648 K), so the real gas effects do not need to be considered. Then the perfect gas assumption is an acceptable condition. Therefore, the perfect gas assumption is utilized in both steps of numerical simulation.

The laminar simulation is used to obtain the steady base flow data of the entire model at different angles of attack. The steady base flow data serve as initial and out-boundary conditions for the transition simulation. The parallel computational fluid dynamics software OpenCFD-EC with finite volume method is used for the laminar simulation. In order to optimize computational resources, the simulation only considers half of the model, with the centerlines of the leeward side and the windward side serving as the symmetry axis. The calculation domain is resolved using 601, 151, and 181 grids in the streamwise, circumferential, and wall-normal directions, respectively, and a total number of grids is  $16.42 \times 10^6$ . The cross-sectional grid distribution is shown in Fig. 3. The inviscid fluxes are computed by using a third-order MUSCL finite difference scheme with a Van Albada limiter, and a Van Leer method is used for flux-vector splitting. The viscous fluxes are computed by using a fourth-order central difference scheme. The time integration is performed using an LU-SGS scheme. At the same flow conditions, the steady base flow is calculated for the HyTRV model at four different angles of attack.

The transition simulation is conducted using the Graphic Processing Unit (GPU)-accelerated finite difference method computational fluid dynamics software OpenCFD-SCU, developed by

Dang *et al.*<sup>38</sup> The software offers a speedup of more than 200 times compared to Central Processing Unit (CPU)-based software using the same algorithm, significantly accelerating the DNS calculation process and reducing computation time. In the transition simulation, the calculation is performed on a small computational domain, with the shock region at the head of the model removed. The calculation range of streamwise direction is  $X \in [30, 1600 \text{ mm}]$ . Two types of grids are used in the calculation, with the same number of grids in each direction, but different in the wall-normal height distribution. The calculation domain is resolved using 4350, 2001, and 161 grids in the streamwise, circumferential and wall-normal directions, respectively, and a total number of grids is  $1.4 \times 10^9$ . In terms of grid distribution, previous studies have found that at the angle of attack of the HyTRV model is greater than  $6^\circ$ , a large vortex is generated near the centerline of the leeward side, while the vortex becomes smaller near the centerline of the windward side.<sup>35</sup> In order to obtain an overall flow field structure at  $7^\circ$  angle of attack, the height of the wall-normal with the near centerline of the leeward side is set increased, while the height of the wall-normal grid with the near centerline of the windward side is set decreased. Nevertheless, the height of the first grid closest to the wall remains consistent between both sets. The specific cross-sectional grid distribution is depicted in Fig. 4.

For the numerical simulation settings of the transition simulation, the isothermal no-slip boundary condition is applied to the wall surface, and the non-reflective outlet boundary condition is applied to the outlet boundary. The inviscid fluxes are computed by using an optimized six-order monotone-preserving scheme (OMP6), proposed by Li *et al.*,<sup>39</sup> and the Steger–Warming method is used for flux-vector splitting. The viscous fluxes are computed by using a sixth-order central difference scheme. The time integration is performed using a third-order total variation diminishing (TVD) type Runge–Kutta scheme. The filtering method proposed by Bogey *et al.*<sup>40</sup> is used to eliminate the high-frequency nonphysical vibrations in the flow field, ensuring the stability of the numerical simulation. The flow field is filtered every 10 steps.

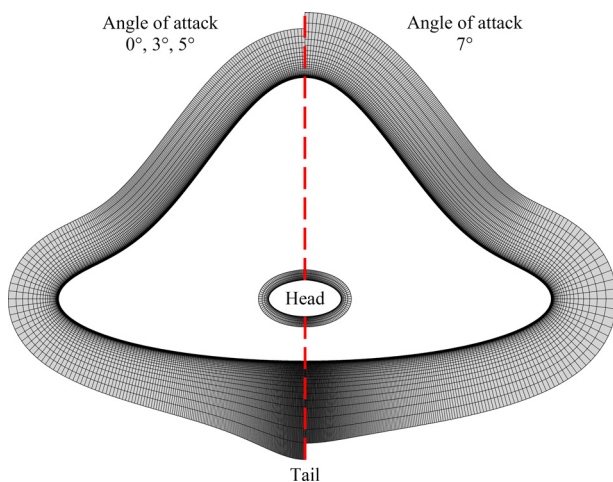


**FIG. 4.** Cross section grid distribution in the transitional simulation at  $X=30$  (head) and  $1500 \text{ mm}$  (tail). The left side of the red dotted line is the grid used by the model at  $0^\circ$ ,  $3^\circ$ , and  $5^\circ$  angle of attack. The right side of the red dotted line is the grid used by the model at  $7^\circ$  angle of attack. For clarity, every fifth grid point is shown in the tail region, and every 20th grid point is shown in the head region.

The boundary layer transition is triggered by continuously introducing random blowing and suction perturbations on the wall of the model within a range of 50–60 mm from the head of the model. The streamwise and circumference velocities are both set as zero on the wall, and the wall-normal velocity on the wall is determined by

$$v_n(x, \phi, t) = \begin{cases} v_0(2\xi - 1), & x_a \leq x \leq x_b, \\ 0, & \text{otherwise,} \end{cases} \quad (4)$$

where  $v_0$  is 2% of the streamwise velocity,  $\xi$  is a random number between 0 to 1, and  $x_a$  and  $x_b$  are the start and end locations of the blowing and suction perturbations, respectively. Previous studies<sup>26,36</sup> have confirmed that the transition can be effectively triggered by introducing these random perturbations. Moreover, the transition location is not sensitive to the specific form perturbations and has a certain universality.

#### D. Grid convergence

In order to verify the grid convergence of the DNS calculation in the transition simulation, four grids with different resolutions are selected for simulation under the flow condition at  $3^\circ$  angle of attack. The specific grid parameters are shown in Table II. Of the four cases, case 1 is the coarsest grid; case 2 has twice as many circumferential grids as case 1; cases 3 and 4 have a finer streamwise grid than case 2; case 4 is the finest grid with a total of  $1.40 \times 10^6$  grids. Compared to the other cases, the grid of case 4 in the wall-normal direction is also refined. The height of the first grid closest to the wall is the same in all cases.

According to the calculation results for transition simulation shown in Figs. 5 and 6, the transition regions are clearly shown by the distribution of the skin friction coefficient. As shown in Fig. 5, for the leeward side, reducing the circumferential grid resolution significantly affects the region 1-L, which may be affected by the cross-flow instability. Therefore, decreasing the circumferential grid resolution can enhance the numerical dissipation of high-frequency disturbances at  $3^\circ$  angle of attack. However, the transition location in this region remains relatively constant compared to other grids with finer resolution. Furthermore, increasing the wall-normal grid resolution will slightly defer the transition, with a more pronounced impact on the region 2-L. On the other hand, the change of the streamwise resolution has minimal effect on the transition for the leeward side.

The effect of grid resolution changes on the windward side is similar to that on the leeward side. As shown in Fig. 6, the region 1-W, which is influenced by cross-flow instability, is greatly affected by the circumferential grid resolution. However, the range and location of the transition have little change. An increase in the wall-normal grid

**TABLE II.** Grid parameters for transition simulation with different grid resolutions.

Case number	Streamwise grids	Circumferential grids	Wall-normal grids	Total grids ( $\times 10^9$ )
Case 1	3000	1001	121	0.36
Case 2	3000	2001	121	0.72
Case 3	4350	2001	121	1.05
Case 4	4350	2001	161	1.40

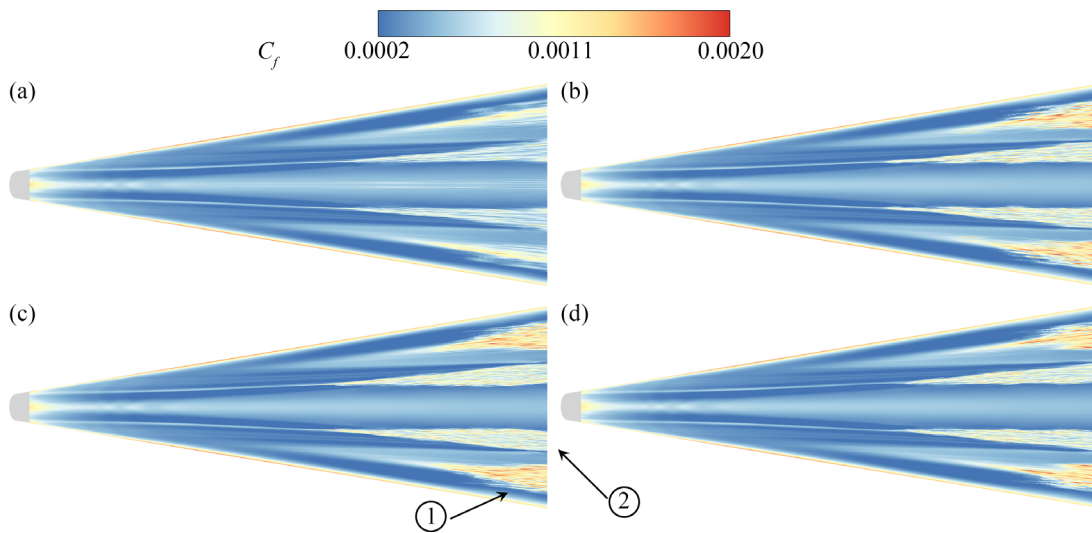


**FIG. 5.** Time-averaged skin friction coefficient distribution on the leeward side with different grid resolutions at 3° angle of attack: (a) case 1, (b) case 2, (c) case 3, (d) case 4, ① region 1-L, ② region 2-L.

resolution can result in a slight delay in the transition of the region 2-W. For the windward side, the change of the streamwise resolution has minimal effect on the transition, similar to that observed on the leeward side.

In order to evaluate the effect of different grid resolutions more thoroughly on the transition, a comparison and verification of the time-averaged skin friction coefficient curves on the centerline of the windward side for the transition simulation with different grid resolutions was conducted. As shown in Fig. 7, it can be observed that the time-average skin friction coefficient with different grid resolutions

fluctuates sharply at  $X = 1100$  mm, indicating that the transition occurs at this location. In addition, the time-averaged skin friction coefficient curves are consistent in the laminar flow region ( $X \in [200, 1100$  mm]). After the transition, the time-averaged skin friction coefficient is mainly concentrated within 0.001–0.0015.

According to the above analysis, the transition ranges and locations with different grid resolutions are generally consistent. Then, this can indicate that the previous grid is sufficient for the use of revealing the transition mechanism. In the transition simulation, the grid parameters in case 4 are selected for calculation.

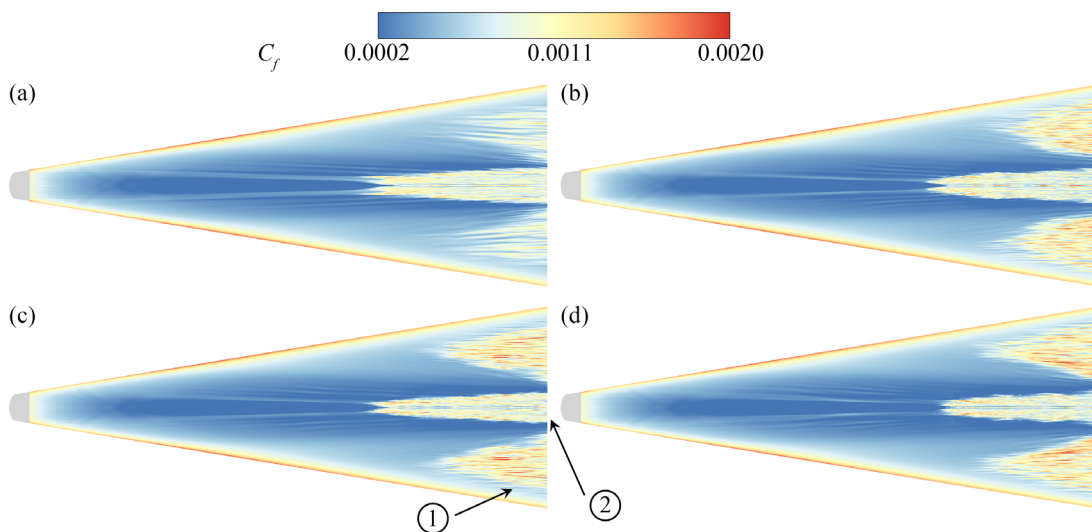


**FIG. 6.** Time-averaged skin friction coefficient distribution on the windward side with different grid resolutions at 3° angle of attack: (a) case 1, (b) case 2, (c) case 3, (d) case 4, ① region 1-W, ② region 2-W.

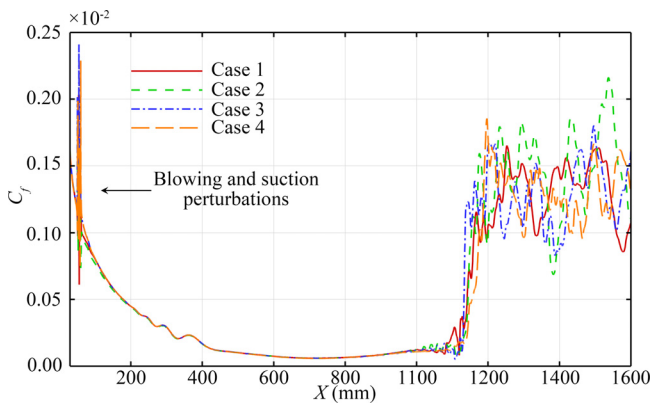


FIG. 7. Time-averaged skin friction coefficient curves on the centerline of the windward side with different grid resolutions at 3° angle of attack.

### III. CALCULATION RESULTS

#### A. Laminar flow pattern

Figure 8 shows the instantaneous pressure distribution of the cross section for the HyTRV model. It is observed that, with the angle of attack increasing, the pressure on the leeward side generally decreases while the pressure on the windward side increases. At 0° angle of attack, there is a high-pressure area above the leeward side (upper surface) of the model and a low-pressure area below the windward side (lower surface) of the model. The pressure at the centerline region of the leeward side is the highest. The pressure from the central line region of the leeward side to the shoulder region of the model decreases first and then increases, resulting in a high-low-high pressure distribution on the leeward side.

As shown in Fig. 8(b), the pressure near the wall of the concave region of the leeward side decrease compared with the surrounding region at 3° angle of attack, which results in a low-pressure area

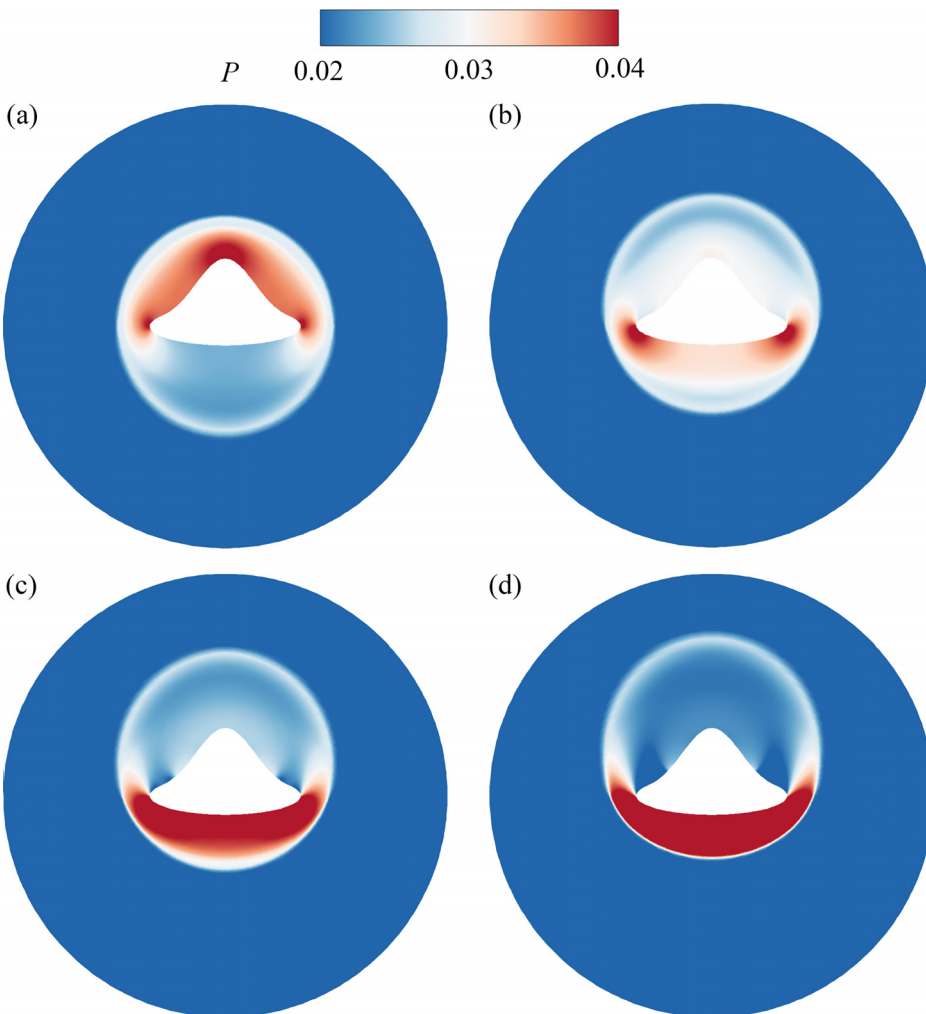


FIG. 8. Instantaneous temperature distribution at different angles of attack for the laminar simulation ( $X = 1500$  mm): (a) 0°, (b) 3°, (c) 5°, and (d) 7°. The trend of the instantaneous temperature distribution with increasing angle of attack is consistent with previous studies.<sup>35</sup>

08 April 2024 03:45:52

generated here. As the angle of attack increases, the pressure of the low-pressure area decreases accordingly, and the range of the low-pressure area gradually expands. As shown in Fig. 8(d), an obvious and large-scale low-pressure area is generated on the concave region of the leeward side at 7° angle of attack. The generation of low-pressure areas may be because, as the angle of attack increases, the flow on the depression of the concave region gradually separates, thus a gradual decrease in the pressure of the area.

Moreover, as the angle of attack increases, the pressure in the shoulder region of the model increases gradually, which results in a high-pressure area generated here. The high-pressure area expands toward the centerline of the windward side. Furthermore, the pressure in the centerline region of the windward side always increases, indicating that the flow in the centerline region is becoming more attached to the surface of the windward side.

According to the above analysis, combined with the streamwise velocity distribution of the HyTRV model in Fig. 9, the generation mechanism of streamwise vortices on the model surface can be found. At 0° angle of attack, the centerline region of the leeward side and the shoulder region of the model have high pressure, while the concave region of the leeward side and the centerline region of the windward side have low pressure. The pressure gradient drives the flow converging from high-pressure areas to low-pressure areas. Streamwise vortices will be generated under the action of shear force, which corresponds to the streamwise vortex observed in the concave region of the leeward side and the centerline region of the windward side at the 0° angle of attack in Fig. 9(a).

As the angle of attack increases, the pressure decreases gradually in the centerline region of the leeward side, and the low-pressure area on the concave region of the leeward side moves toward the centerline of the leeward side. Under the influence of the pressure gradient, the streamwise vortices located on both sides of the model also move

toward the centerline of the leeward side following the low-pressure area. As shown in Fig. 9, the movement of streamwise vortices on both sides of the model is visibly evident. As the angle of attack increases, these streamwise vortices converge as they move upward. As shown in Fig. 9(c), the edges of the streamwise vortices on both sides of the model have connected at 5° angle of attack. However, the centers of these vortices remain separated on both sides of the leeward side's centerline. While in Fig. 9(d), the streamwise vortices on both sides of the model have completely merged to become a large mushroom-shaped streamwise vortex in the central region of the leeward side at 7° angle of attack.

Furthermore, as the angle of attack increases, a new low-pressure area gradually develops in the upper portion of the shoulder region of the model. Under the influence of the pressure gradient, a new flattened streamwise vortex is generated on the new low-pressure area, as observed at 7° angle of attack in Fig. 9(d). The upper edge of the streamwise vortex extends to the top of the model with a significant extension. On the other hand, the lower edge of the streamwise vortex extends to the shoulder of the model with a small extension.

For the centerline region of the windward side, the pressure in this region increases significantly as the angle of attack increases. Simultaneously, the pressure gradient gradually decreases in the centerline region. Consequently, the streamwise vortex in the centerline region of the windward side transforms from a distinct mushroom-like structure, as observed at 0° angle of attack in Fig. 9(a), to a flattened structure, as observed at 7° angle of attack in Fig. 9(d).

In addition, the change of the angle of the shock wave with respect to the axial direction at different angles of attack is still worthy of attention, which is very important for the experimentalists to carry out experimental verification. Figure 10 shows the angle of the shock wave with respect to the axial direction ( $\theta$ ) at different circumferential angles ( $\phi$ ) at different angles of attack ( $X = 20$  mm). Table III shows

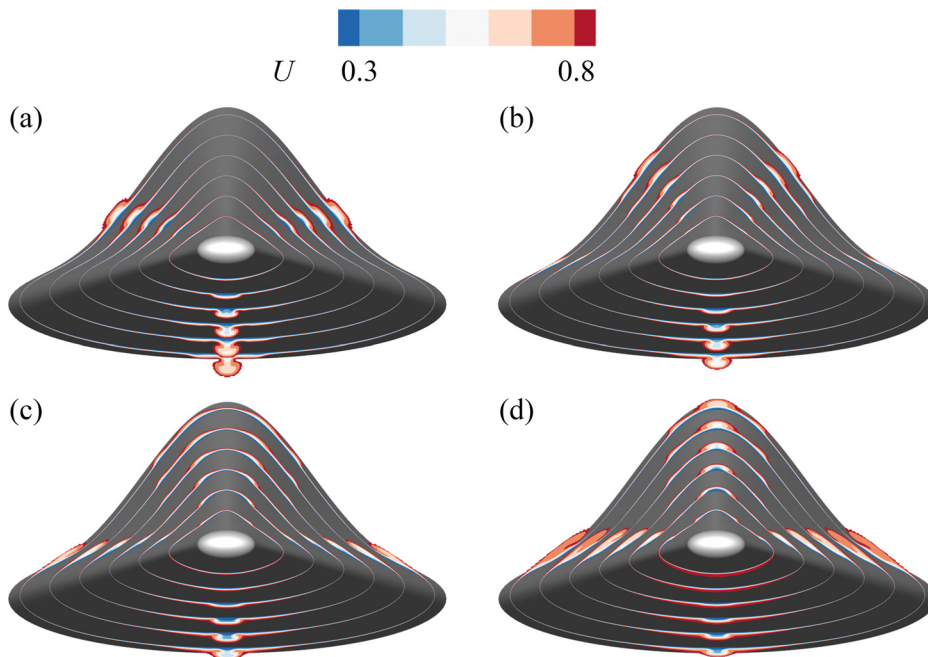


**FIG. 9.** Instantaneous streamwise velocity distribution at different angles of attack for the laminar simulation ( $X = 250, 500, 750, 1000, 1250, 1500$  mm): (a) 0°, (b) 3°, (c) 5°, and (d) 7°. The trend of the instantaneous streamwise velocity distribution with increasing angle of attack is consistent with previous studies.<sup>35</sup>



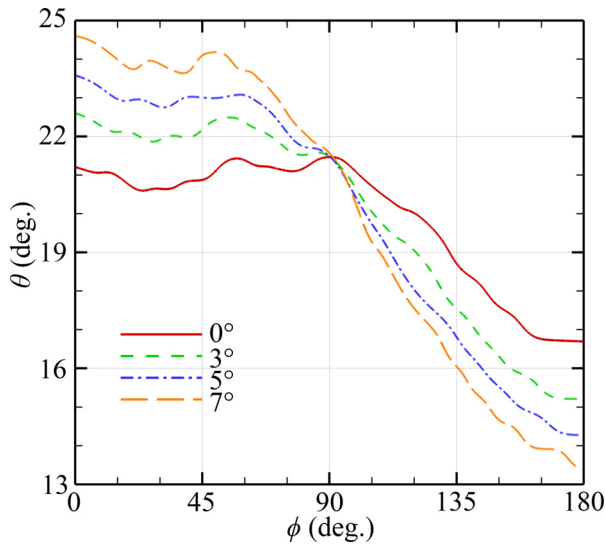


FIG. 10. The angle of the shock wave with respect to the axial direction ( $\theta$ ) at different circumferential angles ( $\phi$ ) ( $X = 20$  mm).

the values of  $\theta$  on some selected regions of interest at different angles of attack. Where  $\phi = 0^\circ, 90^\circ, 180^\circ$  are the circumferential angles of the top, shoulder and bottom of the model, respectively. It can be observed that as the angle of attack increases,  $\theta$  on the leeward side ( $\phi < 90^\circ$ ) gradually increases, while  $\theta$  on the windward side ( $\phi > 90^\circ$ ) gradually decreases. The  $\theta$  of the shoulder ( $\phi = 90^\circ$ ) at different angles of attack varies little, basically around  $21.5^\circ$ .

The above flow characteristics of the laminar simulation of the HyTRV model at different angles of attack are consistent with the findings of previous studies.<sup>35,37</sup> Based on the above analysis, the flow regions of the HyTRV model can be divided as follows. As shown in Fig. 11, the flow region can be divided into seven distinct regions from top to bottom: the leeward attachment-line region, the leeward cross-flow region, the shoulder vortex region, the shoulder cross-flow and vortex region, the shoulder attachment-line region, the windward cross-flow region and the windward vortex region.

It is important to note that the flow region division of the HyTRV model shown in Fig. 11 is not applicable in all cases. As the angle of attack changes, the location and range of the flow region will also change accordingly. As shown in Fig. 9(d), at  $7^\circ$  angle of attack, the leeward attachment-line region and leeward cross-flow region have been replaced by the shoulder vortex region. Therefore, the division of regions at different angles of attack must be determined based on specific circumstances.

TABLE III. The angle of the shock wave with respect to the axial direction ( $\theta$ ) on some selected regions of interest ( $X = 20$  mm).

Angle of attack ( $^\circ$ )	$\phi = 0^\circ$ ( $^\circ$ )	$\phi = 90^\circ$ ( $^\circ$ )	$\phi = 180^\circ$ ( $^\circ$ )
0	21.21	21.47	16.70
3	22.61	21.48	15.22
5	23.58	21.49	14.28
7	24.60	21.57	13.38

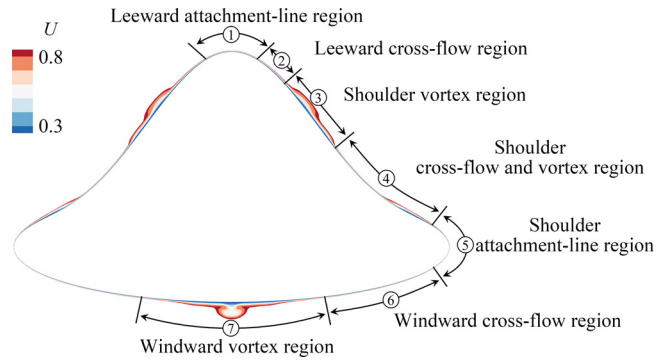


FIG. 11. Flow region division for the laminar simulation. Take the instantaneous streamwise velocity distribution at  $3^\circ$  angle of attack as an example ( $X = 1500$  mm). The region division is similar to that in the previous study.<sup>37</sup> However, the name of the shoulder cross-flow and vortex region is different from the previous study, which is due to a new streamwise vortex generated in the concave region of the leeward side.

B. Transitional flow pattern

The computation for the transition simulation is conducted utilizing the steady basic flow data obtained from the laminar simulation at different angles of attack. Figure 12 shows the instantaneous temperature of the cross section for the HyTRV model. Compared with the results for laminar flow simulation in Fig. 9, it can be observed that the shoulder vortex region and the windward vortex region at each angle of attack have transitioned due to streamwise vortex instability. Furthermore, streamwise vortex instability is more obvious in the shoulder cross-flow and vortex region since the  $3^\circ$  angle of attack.

As the angle of attack increases, the streamwise vortices in the shoulder vortex region on both sides of the model gradually move to the centerline region of the leeward side and merge. At  $7^\circ$  angle of attack, the streamwise vortices located on both sides of the model merge into a whole vortex, which subsequently breaks away from the model's surface. The shape of the streamwise vortices in the windward vortex region gradually become flattened. The streamwise vortex instability on the centerline of the windward vortex region is the strongest, while the instability tends to weaken toward the two sides of the model. The streamwise vortex of the shoulder cross-flow and vortex region becomes larger gradually as the angle of attack increases. Following destabilization, the streamwise vortex progressively detaches to the upper part of the model along the wall.

In previous studies,<sup>36,37</sup> the distribution of the skin friction coefficient can be regarded as the reflection of the transition region. Hence, to further study the transition in each region of the HyTRV model, the distribution of the time-averaged skin friction coefficient is utilized to divide the transition regions, which are shown in Fig. 13. The skin friction coefficient can be defined as follows:

$$C_f \equiv |2\mu\nabla\bar{U}|_w/R. \tag{5}$$

According to the division depicted in Fig. 11, the boundary layer transition occurs in four specific regions of the model: the shoulder cross-flow and vortex region and the shoulder vortex region on the leeward side; the windward vortex region and the windward cross-flow region on the windward side.

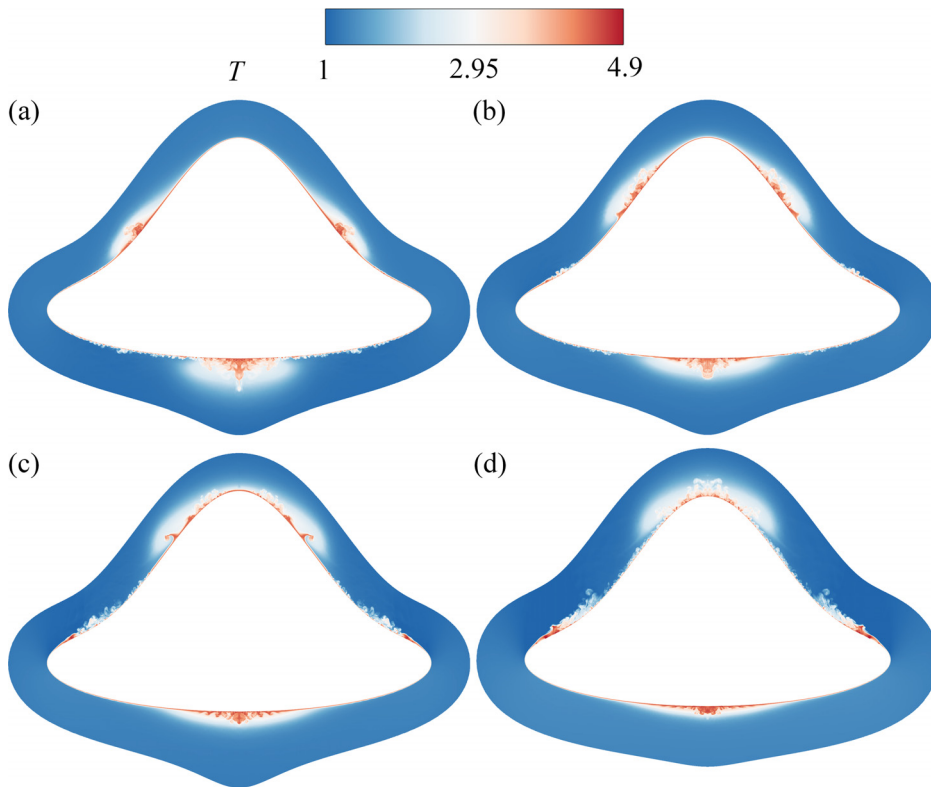


**FIG. 12.** Instantaneous temperature distribution at different angles of attack for the transition simulation ( $X = 1500$  mm): (a)  $0^\circ$ , (b)  $3^\circ$ , (c)  $5^\circ$ , and (d)  $7^\circ$ .

The time-averaged skin friction coefficient distribution of the HyTRV model, which is shown in Figs. 14 and 15, clearly shows the range and location of transition for each transition region at different angles of attack. It is observed that the transition region for each angle of attack exhibits a triangular shape. As the angle of attack increases, the range and location of the transition in each region significantly change.

As shown in Fig. 16, a comparison of the time-averaged skin friction coefficient curves at various angles of attack reveals that the transition on the centerline of the windward vortex region is gradually

delayed as the angle of attack increases. Specifically, the transition occurs at  $X = 800$  mm at  $0^\circ$  angle of attack. However, as the angle of attack increases, the transition location is delayed to  $X = 1400$  mm at  $7^\circ$  angle of attack. Furthermore, it can be observed that the time-averaged skin friction coefficient experiences only a slight variation at the later stage of transition as the angle of attack increases. The time-averaged skin frictions are approximately coefficient consistent at different angles of attack, mainly located in 0.001–0.0015.

After completing the general analysis of transition flow patterns at different angles of attack, the following will delve into a more specific analysis of the four transition regions.

### C. Shoulder cross-flow and vortex region

As shown in Fig. 14, with the angle of attack increasing, the transition location of the shoulder cross-flow and vortex region moves gradually forward, and the range of the transition also extends gradually.

Figure 17 shows the head of the shoulder cross-flow and vortex region at different angles of attack. It is observed that there are multiple transversal bands (perpendicular to streamwise direction) with equal spacing within the transition region at  $0^\circ$  angle of attack. According to a previous study,<sup>37</sup> they may originate in Mack instability. Moreover, compared to the time-averaged skin friction coefficient distribution in Fig. 14, the transition region does not exhibit any visible bands, indicating that these transversal bands (seen from Fig. 17) are likely associated with traveling cross-flow waves. As the angle of attack increases, the transversal bands in the interior of the transition region

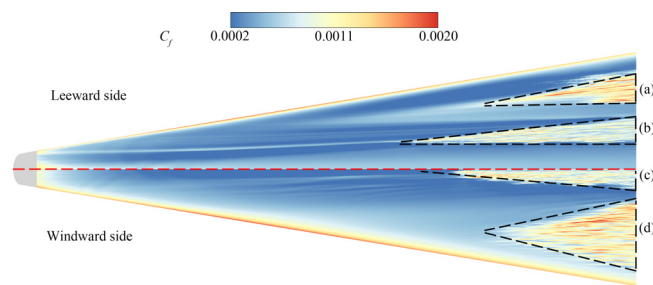


**FIG. 13.** Transition region division for the transition simulation. Take the time-averaged skin friction coefficient distribution at  $3^\circ$  angle of attack as an example. Take the centerline of the model as the boundary. The upper part of the figure is the region division on the leeward side, and the lower part is the region division on the windward side: (a) shoulder cross-flow and vortex region, (b) shoulder vortex region, (c) windward vortex region, and (d) windward cross-flow region.

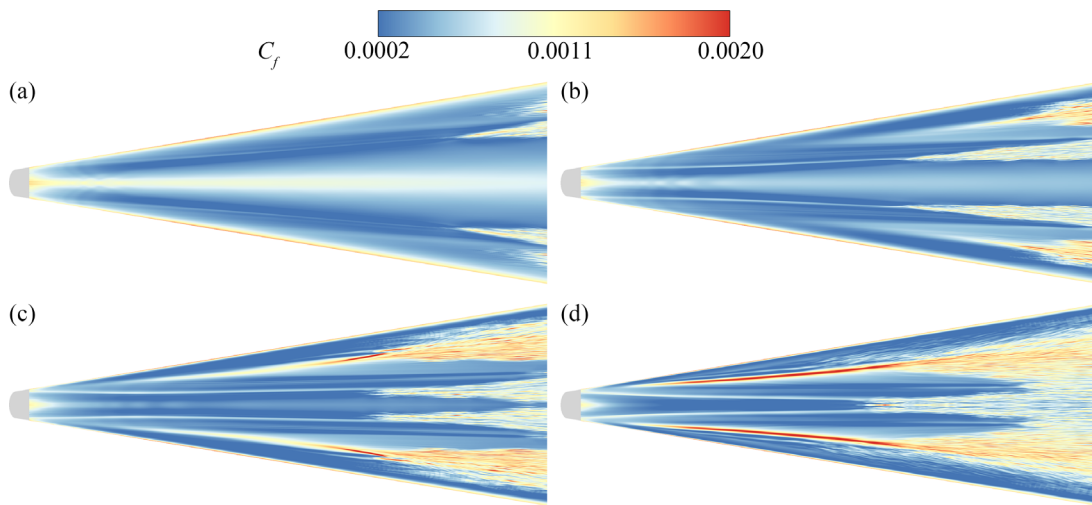


**FIG. 14.** Time-averaged skin friction coefficient distribution on the leeward side at different angles of attack for the transition simulation: (a) 0°, (b) 3°, (c) 5°, and (d) 7°.

gradually disappear. The bands are primarily distributed on the exterior of the transition region, close to the shoulder attachment line of the model. It is noteworthy that, as the angle of attack increases to 5° and 7°, a long section of high skin friction coefficient region (hereafter referred to as the H- $C_f$  region) appears at the head of the transition region, which exhibits a long strip shape and not shown at 0° and 3° angles of attack. The region's tail is destabilized and connected to the head of the triangular transition region.

In order to determine the range of the transition region, it is defined as follows: The actual transition region is demarcated by the 40% contour line of the maximum time-averaged skin friction coefficient within the transition region at each angle of attack. Other transition regions are defined similarly to this region.

For the shoulder cross-flow and vortex region, the H- $C_f$  region at the head of the transition region will affect the determining of the

transition location. Therefore, at 5° and 7° angles of attack, it is defined that the actual H- $C_f$  region is demarcated by the 60% contour line of the maximum time-averaged skin friction coefficient within each H- $C_f$  region. The location of the H- $C_f$  region's tail represents the actual transition location. Furthermore, at 7° angle of attack, the shoulder cross-flow and vortex region and the shoulder vortex region are connected at their tail, which results in the inability to determine the range of the transition region. Therefore, the shared border of these two transition regions is utilized to demarcate the range of the transition region.

Table IV shows the coordinates of the head and tail of the H- $C_f$  region. Through analyzing the location of the H- $C_f$  region at different angles of attack, it is observed that the angle of attack significantly affects the direction and the length of the H- $C_f$  region. As shown in Table V, with the angle of attack increasing, the angle between head-

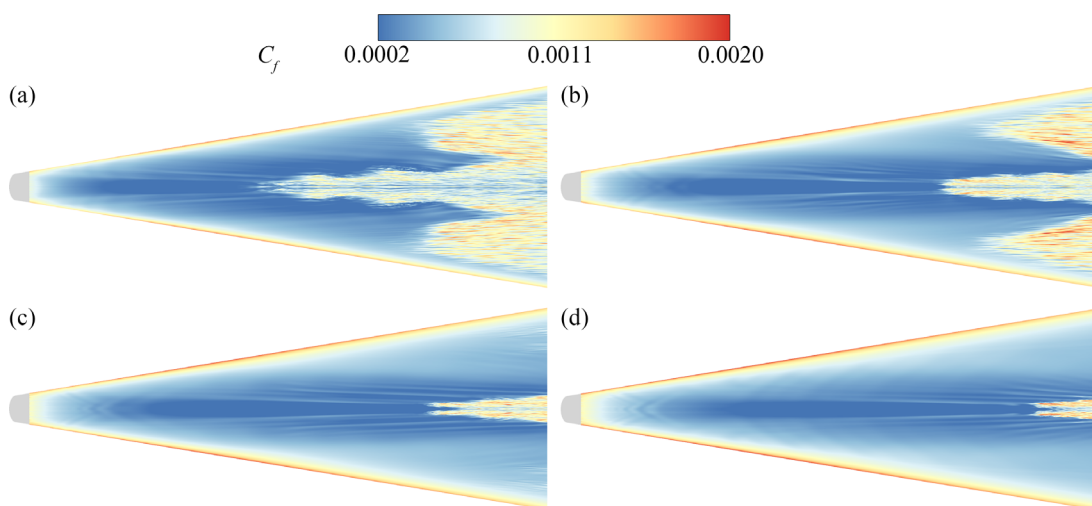


**FIG. 15.** Time-averaged skin friction coefficient distribution on the windward side at different angles of attack for the transition simulation: (a) 0°, (b) 3°, (c) 5°, and (d) 7°.

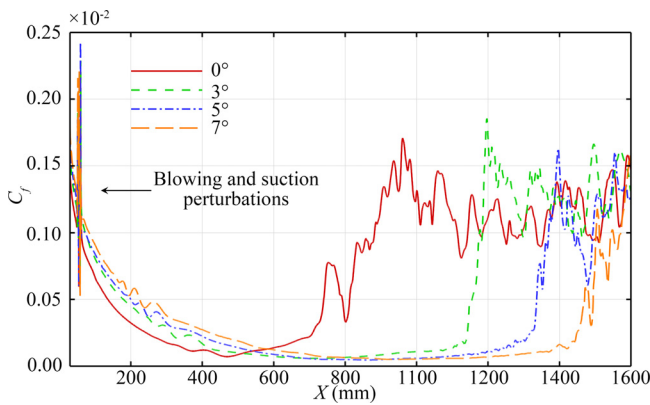


FIG. 16. Time-averaged skin friction coefficient curves on the centerline of the windward side at different angles of attack for the transition simulation.

to-tail connecting line of the H- $C_f$  region and the centerline of the model decreases, while the length of the region increases significantly. Furthermore, the maximum time-averaged skin friction coefficient in this region will increase as the angle of attack increases.

Table VI shows the transition region data of the shoulder cross-flow and vortex region. The transition locations at 5° and 7° angles of attack have been replaced by the tail locations of the H- $C_f$  region. According to the obtained data, as the angle of attack increases, the transition location of the shoulder cross-flow and vortex region moves forward at a decreasing rate, while the width for the tail of the transition region expands at an increasing rate. It is noteworthy that  $C_{fmax}$  and  $Y_{t-o}$  increase at 0° to 5° angles of attack but decrease at 7° angle of attack.

TABLE IV. H- $C_f$  region locations at different angles of attack.

Direction	Head (5°, mm)	Tail (5°, mm)	Head (7°, mm)	Tail (7°, mm)
X	992.654	1120.75	407.65	1008.53
Y	131.47	153.50	68.46	122.38
Z	53.98	52.29	31.17	64.31

TABLE V. H- $C_f$  region data at different angles of attack.  $C_{fmax}$  is the maximum value for the time-averaged skin friction coefficient in the H- $C_f$  region.

Angle of attack (°)	$C_{fmax}$ ( $\times 10^{-2}$ )	The angle to the centerline (°)	Length (mm)
5	0.3001	9.79	129.99
7	0.3213	6.01	604.20

To further analyze the situation in this transition region, 3° and 7° angles of attack have been chosen as representative cases for analysis. Figure 18 shows the instantaneous skin friction coefficient distribution on the leeward side at two angles of attack. In addition, two regions of interest, zones A and B, are selected in the transition regions of 3° and 7° angles of attack with black dotted lines, respectively. Figures 19 and 20 show the instantaneous flow pattern in the zones A and B, respectively, where the vortex structures are illustrated using the Q-criterion proposed by Hunt *et al.*<sup>41</sup>

As shown in Fig. 19, the vortices in this transition region initially manifest as oblique rolls (like the structure in the red solid line area) with a consistent azimuth angle and equal spacing at 3° angle of attack.

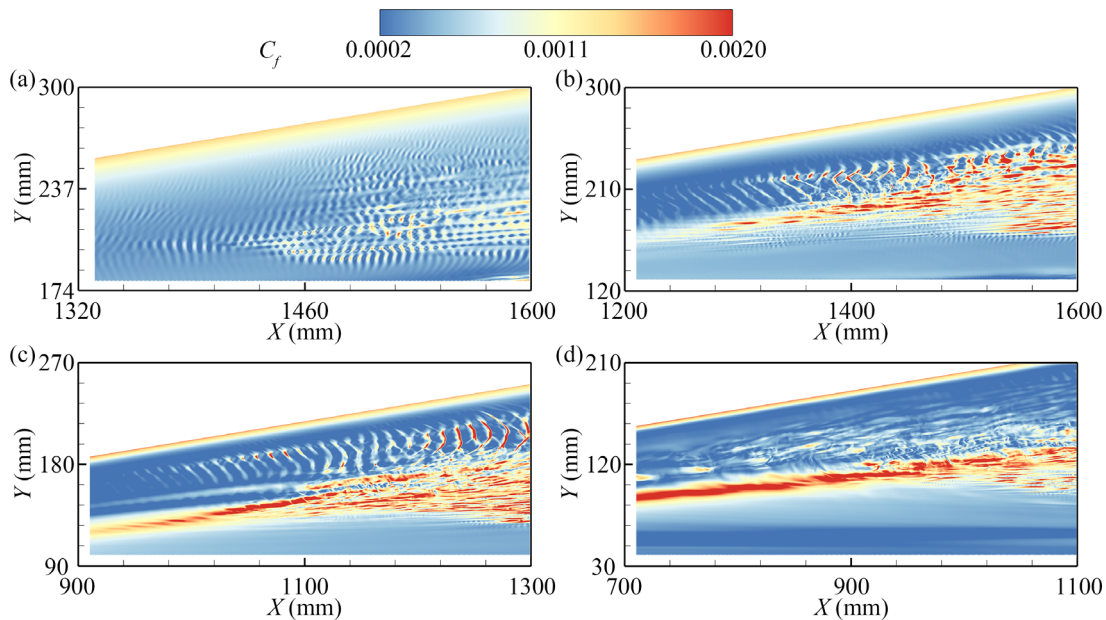
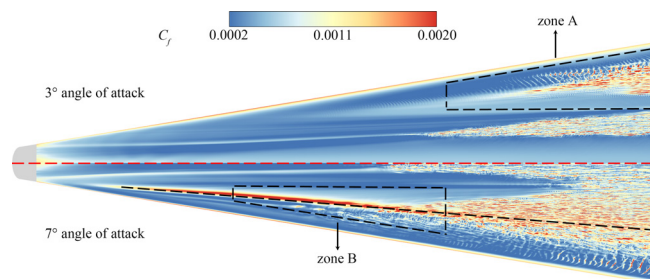


FIG. 17. Instantaneous skin friction coefficient distribution at the head of the shoulder cross-flow and vortex region at different angles of attack: (a) 0°, (b) 3°, (c) 5°, and (d) 7°.

**TABLE VI.** Transition region data of the shoulder cross-flow and vortex region at different angles of attack.  $C_{fmax}$  is the maximum value for the time-averaged skin friction coefficient in the transition region;  $X_{head}$  is the X axis value of the transition location;  $Y_{L,i}$  and  $Y_{L,o}$  is the Y axis value of the transition region's tail on the side close to the model centerline (inside) and away from the model centerline (outside) at the  $X = 1600$  mm section, respectively;  $Y_w = Y_{L,o} - Y_{L,i}$  is used to indicate the width of the transition region's tail.

Angle of attack ( $^\circ$ )	$C_{fmax}$ ( $\times 10^{-2}$ )	$X_{head}$ (mm)	$Y_{L,i}$ (mm)	$Y_{L,o}$ (mm)	$Y_w$ (mm)
0	0.2022	1522.81	201.20	246.54	45.34
3	0.2218	1233.11	171.43	250.28	78.85
5	0.2384	1120.75	135.10	252.71	117.61
7	0.2103	1008.53	69.28	239.26	169.98



**FIG. 18.** Instantaneous skin friction coefficient distribution. Divided by the centerline of the model, the upper part of the figure is the leeward side at  $3^\circ$  angle of attack, and the lower part is the leeward side at  $7^\circ$  angle of attack.

Moreover, these oblique rolls are arranged in multiple longitudinal bands along the streamwise direction, and are more particularly obvious at the edge of the transition region. With the development of oblique rolls,  $\Lambda$  vortices gradually emerge and transition, eventually merging with other surrounding oblique rolls to form a triangular region. It is also observed that the vortices within the range indicated by the black dotted line in Fig. 19 are larger than those in the surrounding areas. Comparison with Fig. 12 reveals that as the angle of

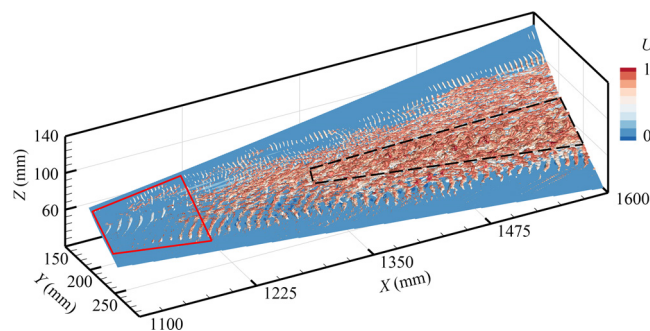


**FIG. 19.** Instantaneous flow pattern in the zone A at  $3^\circ$  angle of attack. The lower part of the figure is the wall-normal section (at the 10th grid point from the wall) represented by the streamwise velocity, and the upper part is the instantaneous vortex structure showed by the isosurface of the Q-criterion ( $Q = 0.001$ ) colored by the streamwise velocity.

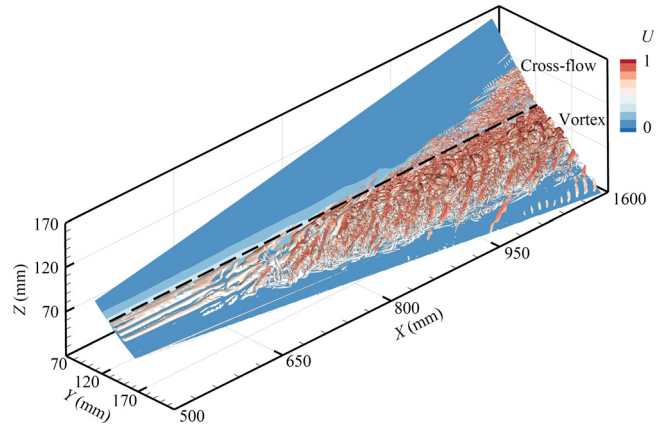


**FIG. 20.** Instantaneous flow pattern in the zone B at  $7^\circ$  angle of attack (same settings as Fig. 19).

attack increases, the black dotted line area expands rapidly and a streamwise vortex develops in this area.

As shown in Fig. 20, the long black dotted line on the leeward side at  $7^\circ$  angle of attack in the lower part of Fig. 18 corresponds to the black dotted line in Fig. 20, which is used to divide the region of cross-flow instability and the region of streamwise vortex instability. Compared with Fig. 19, it can be observed that the black dotted line area in Fig. 19 has developed into a large-scale streamwise vortex at  $7^\circ$  angle of attack. The streamwise vortex is initially stable but becomes unstable at  $X = 700$  mm. With the development of the streamwise vortex, the cross-flow instability in the upper portion of the transition region intensifies and a transition occurs at  $X = 900$  mm. The boundary between the upper cross-flow instability region and the lower streamwise vortex instability region can be distinguished by the extension line of the upper edge of the streamwise vortex, as depicted by the long black dotted line in Figs. 18 and 20.

Figure 21 shows the projection of the streamlines and pressure distribution at  $X = 700$  mm with  $7^\circ$  angle of attack. It can be observed

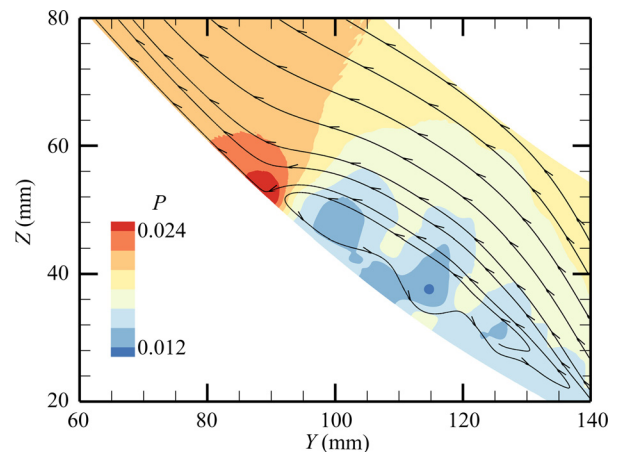


**FIG. 21.** Distribution of instantaneous pressure and streamlines in the zone B at  $7^\circ$  angle of attack (the projection at  $X = 700$  mm).

that the rapid change in the direction of the flow near the wall above the flow vortex, resulting in the formation of a high-pressure area at the location of this change. Under the influence of pressure gradient, the velocity gradient will increase, which results in an increase in the skin friction coefficient. Moreover, the streamwise vortex experienced a long period of stable flow at the initial stage, resulting in the formation of the H- $C_f$  region. As the angle of attack increases, changes in the length and direction of the streamwise vortex also lead to corresponding changes in the location and range of the H- $C_f$  region.

Previous research<sup>36</sup> suggested that at 0° angle of attack, the transition of the shoulder cross-flow and vortex region is caused by the cross-flow instability between the shoulder attachment line and the shoulder vortex region. As the angle of attack increases, this cross-flow instability is strengthened and the range of transition expands. However, the streamwise vortex is gradually generated with the expansion of the low-pressure area on concave region of the leeward side. At small angles of attack, the region of streamwise vortex instability is small, and is surrounded by a larger region of cross-flow instability, which is shown in Fig. 19. However, as the angle of attack increases, the range of the streamwise vortex instability region gradually expands. The entire transition region is divided into three parts:

- (a) The cross-flow instability region in a small range from the shoulder attachment line to the outside of the newly generated streamwise vortex.
- (b) The newly generated streamwise vortex instability region.
- (c) An extensive range of cross-flow instability regions from the streamwise vortices to the concave region of the model and its upper part.

It is noteworthy that the height of the flow vortex from the wall of the model is high, resulting in the actual boundary layer transition region being smaller than the entire streamwise vortex instability region. Figure 22 shows the instantaneous flow pattern at the tail of the shoulder cross-flow and vortex region at 7° angle of attack. It can be clearly observed the three parts of the transition region mentioned above. Comparing the transition region at 7° angle of attack in Figs. 18 and 22, it can be observed that the streamwise vortex region at the tail

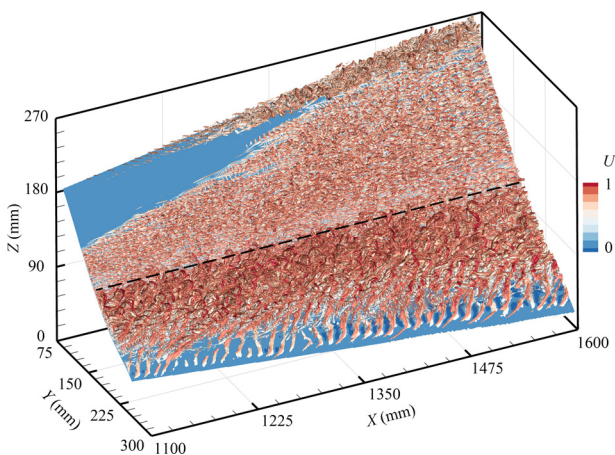


FIG. 22. Instantaneous flow pattern at the tail of the shoulder cross-flow and vortex region at 7° angle of attack (same settings as Fig. 19).

of the transition region has completely transitioned and exhibits an extensive range.

#### D. Shoulder vortex region

As shown in Fig. 14, with the angle of attack increasing, the shoulder vortex region consistently moves toward the centerline of the leeward side under the influence of the streamwise vortex. The transition location moves forward obviously in the range of angles of attack between 0° and 3°, but this movement is less pronounced between 3° and 7° angles of attack.

The definition and parameters of the shoulder vortex region are similar to those of the shoulder cross-flow and vortex region (seen from Sec. III C). A comparison of the data presented in Table VII (the definitions of parameters are the same as that in Table VI) reveals that as the angle of attack increases,  $C_{fmax}$  consistently increases, while the transition location does not exhibit a monotonic increase. The transition location ( $X_{head}$ ) moves rearward between 3° and 5° angles of attack. In addition, it can be observed that the tail of the transition region ( $Y_{t,i}$ ) has moved to the centerline of the leeward side ( $Y = 0$  mm) at 7° angle of attack, indicating that the shoulder vortex regions on both sides of the centerline of the leeward side have merged, which is shown in Fig. 14(d). Following the merger of the transition regions, the disturbance within the transition region is enhanced, which may lead to a forward movement of the transition location at 7° angle of attack as compared to that at 5° angle of attack. The width of the tail of the transition region ( $Y_w$ ) consistently shows an increasing trend with the angle of attack increases.

As illustrated in Figs. 23(a) and 23(b), the shape of the transition region's head is sharp at 0° and 3° angle of attack. The skin friction coefficient along the direction of the azimuth angle extension line is high, extending to both sides of the model's head as shown in Fig. 14. However, the shape of the transition region's head is flat and wide at 5° and 7° angles of attack. Upon observation, the head of the transition region at 5° and 7° angles of attack can be divided into two areas by the red dotted line in Figs. 23(c) and 23(d):

- (a) The outside area (above the red dotted line) of the transition region's head exhibits similar characteristics to the transition region's head observed above at 0° and 3° angles of attack.
- (b) The inside area (below the red dotted line) of the transition region's head is wider and shorter than the outside area.

Moreover, there are multiple transversal bands in front of the inside area of the transition region's head at 5° angle of attack, which is shown in Fig. 23(c). As solid red lines shown in Figs. 23(a)–23(d), there is a distinct boundary of the skin friction coefficient between the

TABLE VII. Transition region data of the shoulder vortex region at different angles of attack.

Angle of attack (°)	$C_{fmax}$ ( $\times 10^{-2}$ )	$X_{head}$ (mm)	$Y_{t,i}$ (mm)	$Y_{t,o}$ (mm)	$Y_w$ (mm)
0	0.1781	1330.75	137.9	181.71	43.81
3	0.1805	973.20	72.76	128.74	55.98
5	0.2079	1094.73	10.69	78.90	68.21
7	0.2159	913.48	0.00	69.28	69.28

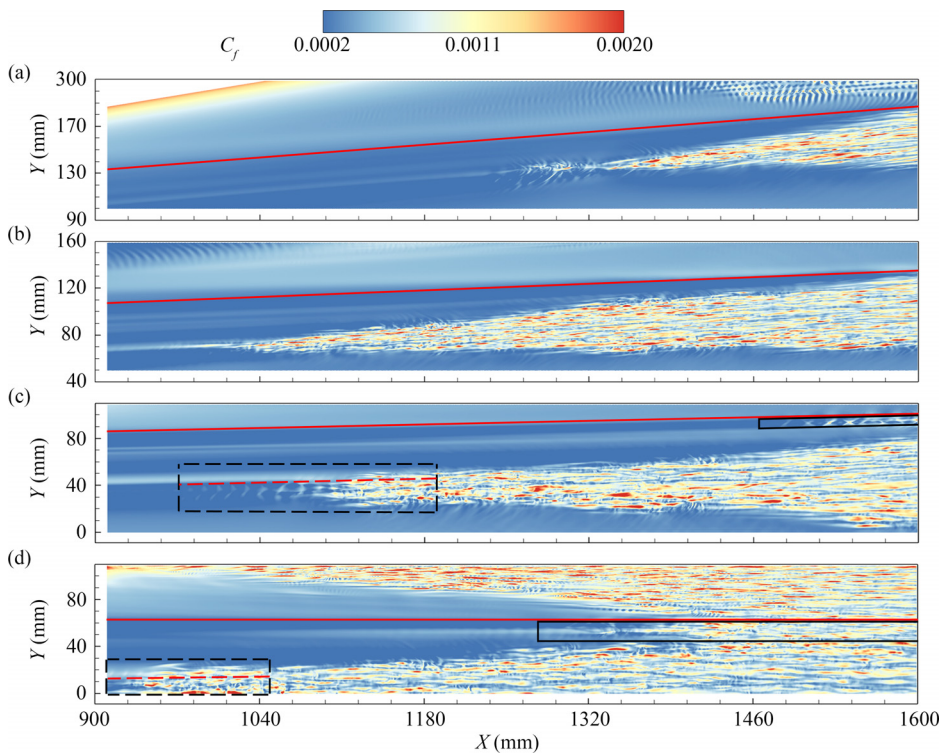


**FIG. 23.** Instantaneous skin friction coefficient distribution of the shoulder vortex region at different angles of attack: (a) 0°, (b) 3°, (c) 5°, and (d) 7°.

shoulder vortex region and the shoulder cross-flow and vortex region. The region around the shoulder cross-flow and vortex region is above the solid red line, and the region around the shoulder vortex region is below the solid red line. In particular, the skin friction coefficient around the shoulder cross-flow vortex region is higher than around the shoulder vortex region. The angle between the boundary line and the centerline of the model decreases as the angle of attack increases.

It is noteworthy that as the angle of attack increases, a new transition region emerges between the tail of two transition regions on the leeward side at 5° and 7°, which is shown in the black solid line area in Figs. 23(c) and 23(d). The new transition region has a narrow width and length of the region increases as the angle of attack increases. Furthermore, at 7° angle of attack, the new transition region is sandwiched between the upper cross-flow instability region and the lower streamwise vortex instability region, connecting the three transition regions. In addition, it can be observed that the transition region moves to the centerline of the windward side at 7° angle of attack [seen from Fig. 23(d)]. It indicates that the transition regions on both sides of the centerline of the leeward side have mostly merged into one.

Figure 24 shows the vortex structure of the shoulder vortex region at 3° angle of attack, with the head structure of the disturbance magnified in the upper left corner of the figure. It can be observed that the disturbance is present throughout the head of the vortex, approximately around  $X = 820$  mm. Initially, the disturbance appears as some small crescent-shaped vortices. As the disturbance develops, the crescent-shaped vortex gradually grows. Within the range of  $X = 900\text{--}1000$  mm, the top of crescent-shaped vortices is stretched and broken, then rapidly contaminating the whole streamwise vortex

area. The transition location observed is mainly consistent with those in Table VII.

As shown in Fig. 25, based on the vortex structure of the disturbance's head at 5° angle of attack, it can be distinctly divided into two disturbance areas: inside and outside. The two disturbance areas are consistent with two areas on the transition region's head observed in Fig. 23(c). The outside area (with a large  $Y$ ) of the disturbance's head

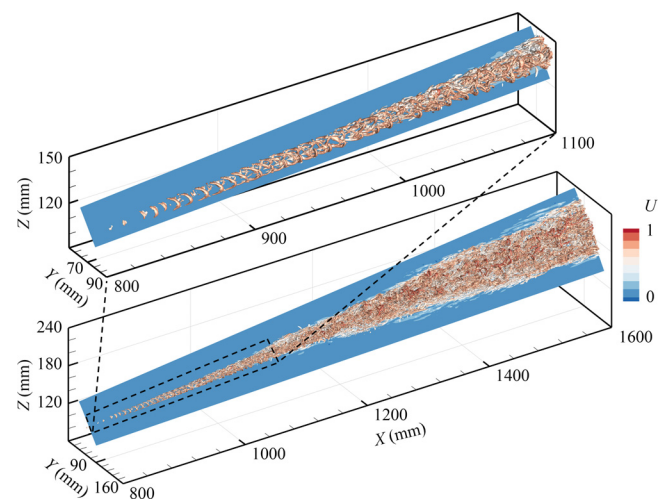


**FIG. 24.** Instantaneous flow pattern of the shoulder vortex region at 3° angle of attack (same settings as Fig. 19).

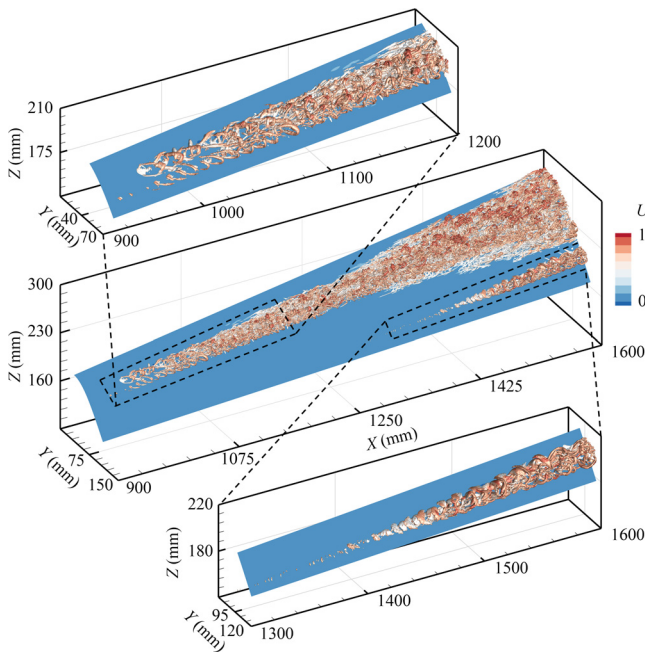


**FIG. 25.** Instantaneous flow pattern of the shoulder vortex region at 5° angle of attack (same settings as Fig. 19).

at 5° angle of attack is similar to that at 3°. However, the development of the crescent-shaped vortex at the front of the disturbance is significantly faster than that at 3° angle of attack, and the width of the crescent-shaped vortex is broader with a flat shape. The inside area (with a small  $Y$ ) of the disturbance’s head presents a flat ring-shaped vortex composed of upper and lower crescent-shaped vortices. With the development of the disturbance, the ring-shaped vortex gradually breaks and connects with the outer crescent-shaped vortex. Subsequently, the two kinds of vortices gradually merge into one and occur transition rapidly.

As depicted by the streamlines (black lines) near the wall on the leeward side in Fig. 26, it can be observed that, the flow from the head area of the centerline of the leeward side and the attachment line of

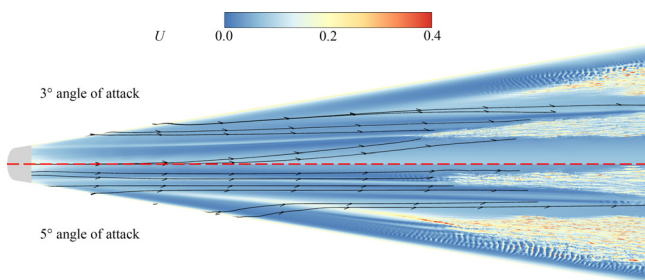


**FIG. 26.** Instantaneous streamwise velocity distribution of the leeward side at different angles of attack, depicted by a wall-normal slice (at the 10th grid point from the wall): Take the centerline of the model as the boundary. The upper part of the figure is the simulation at 3° angle of attack, and the lower part is the simulation at 5° angle of attack.

the shoulder converges in the shoulder vortex region. Under the influence of shear force, the streamwise vortex becomes unstable and occurs in transition. In addition, the streamwise vortex instability region is a sharp shape and a long length at 3° angle of attack, which is due to the large angle and broad range of flows in both directions. However, at 5° angle of attack, the streamline at the head area of the centerline on the leeward side begins to diverge to the outside of the mode’s head, and the streamline at the head area of the shoulder attachment line is sparser than that at 3° angle of attack. It indicates that the flow of the model’s head is gradually separated. Consequently, the angle between the flows in the two directions on the outside of the disturbance’s head becomes smaller, and delaying the flow convergence. This change in flow may cause the transition location to move backward compared to the 3° angle of attack. Moreover, the gradual instability of the flow along the streamline in front of the transition region may cause the ring-shaped vortex inside the disturbance head.

Furthermore, in the lower part of Fig. 25, it is observed that a new streamwise vortex instability region is generated, which is corresponding to the black solid line area of Fig. 23(c). The disturbance initially shows as some small vortices, which subsequently evolved into a larger crescent-shaped flat vortex. In addition, the transition approximately occurs around  $X = 1500$  mm. As shown in Fig. 27, under the influence of the streamwise vortex in the shoulder cross-flow and vortex region, the flow above the streamwise vortex gradually converges close to the wall, which can enhance the cross-flow in that area. The cross-flow above the shoulder cross-flow and vortex region and the streamwise flow below the shoulder vortex region converge between the tails of two transition regions, which generate the disturbance and flow instability, further resulting in the occurrence of transition.

As shown in the vortex structure in Fig. 28, the tail of the streamwise vortex instability region in the upper part of the transition region has fully merged with the new instability streamwise vortex region in the lower part of the transition region at 7° angle of attack. The merged streamwise vortex instability region and the cross-flow instability region of the shoulder cross-flow and vortex region are connected at their tail, and a distinct boundary can be observed.

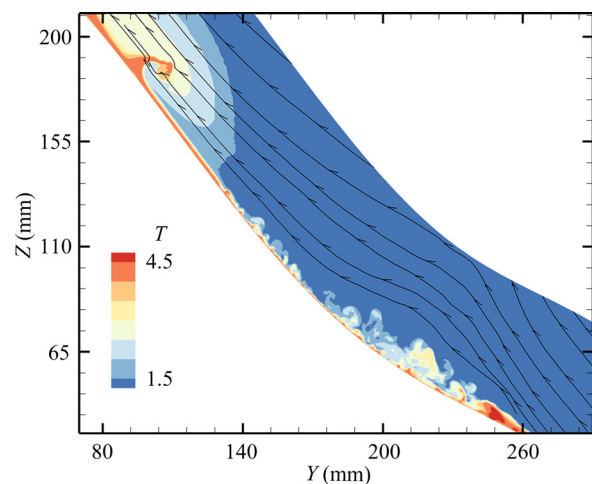


**FIG. 27.** Distribution of instantaneous temperature and streamline in the transition region at 5° angle of attack (the projection at  $X = 1500$  mm).

08 April 2024 03:45:52



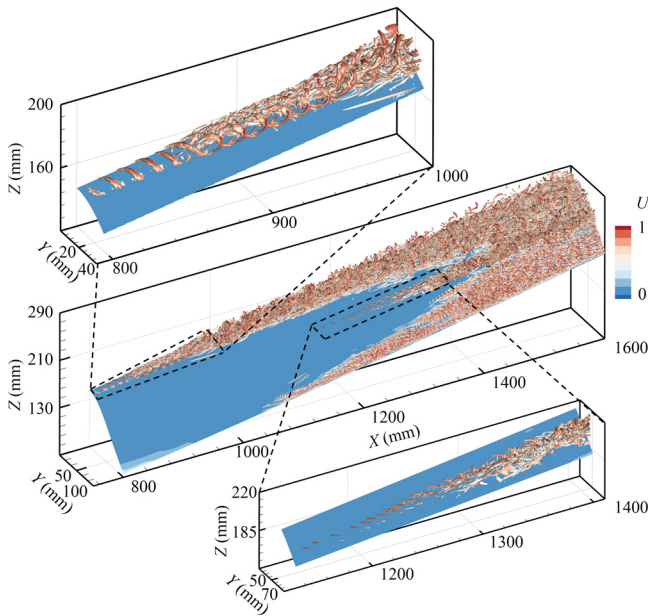


FIG. 28. Instantaneous flow pattern of the shoulder vortex region at 7° angle of attack (same settings as Fig. 19).

Moreover, the crescent-shape vortex at the head of the upper streamwise vortex instability region at 7° angle of attack is wider and flatter than that of the shape observed at 5° angle of attack. It can also be observed that, the disturbance at 7° angle of attack develops faster than that at 3° and 5° angles of attack. In addition, the ring-shaped vortex, which is similar to the vortex on the outside area of the disturbance head at 5° angle of attack, connects with the tail of the crescent-shaped vortex. As for the new region of streamwise vortex instability in the lower part of Fig. 28, small oblique rolls with similar spacing are present in the head of the disturbance. These rolls are believed to be generated by traveling cross-flow waves, which are considered the

TABLE VIII. Transition region data of the windward vortex region at different angles of attack.

Angle of attack (°)	$C_{fmax} (\times 10^{-2})$	$X_{head}$ (mm)	$Y_t$ (mm)
0	0.1870	784.69	79.77
3	0.1941	1133.02	53.48
5	0.1892	1250.50	39.39
7	0.2245	1409.73	28.25

consequence of the further enhanced cross-flow around the shoulder cross-flow and vortex region.

### E. Windward vortex region

As shown in Fig. 15, with the angle of attack increasing, the range of the windward vortex region decreases with the shrinking of the streamwise vortex. The definition of the windward vortex region is similar to that of the two transition regions on the leeward side (seen from Sec. III C). Since the transition region is located on the centerline of the windward side, the width of the transition region is represented by the value of the Y axis outside the tail of the transition region ( $Y_t$ ) (the definitions of other parameters are the same as that in Table VI). As shown in Table VIII, it can be found that as the angle of attack increases,  $C_{fmax}$  shows an increasing trend. However, the length and width of the transition region are consistently decreasing.

Figure 29 shows the windward vortex region at different angles of attack by instantaneous skin friction coefficient distribution. As the angle of attack increases, the transition spots of high skin frictional coefficients tend to be denser, indicating an increase in the average skin frictional coefficient. This can be attributed to the increase in the angle of attack, which enables the pressure to increase continuously in the windward vortex region and the flow in the region and the vortex are close to the wall. Moreover, as the angle of attack increases, the boundary of the transition region gradually transforms from rough to smooth. This suggests that other transitions may occur beyond the

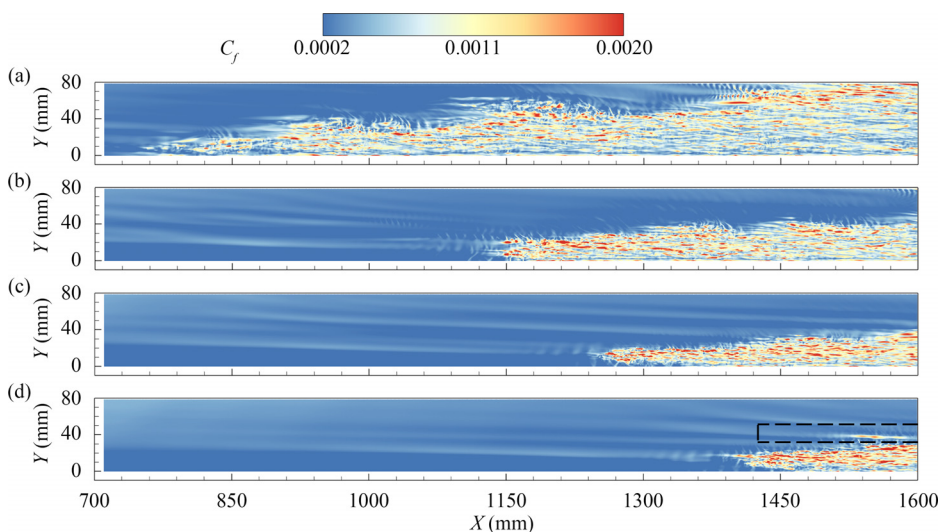


FIG. 29. Instantaneous skin friction coefficient distribution of the windward vortex region at different angles of attack: (a) 0°, (b) 3°, (c) 5°, and (d) 7°.

boundary of the transition region. In addition, a new transition region appears outside the tail of the original transition region at  $7^\circ$  angle of attack, which is shown in the black dotted line area on the right side of Fig. 29(d).

Since the windward vortex region shows a monotonic change as the angle of attack increases in Fig. 29, the windward vortex region at the  $0^\circ$  and  $7^\circ$  angles of attack with significant differences have been selected for further analysis. As shown in Fig. 30, the windward vortex region originated from the streamwise vortex instability. It can also be observed that, the development's speed of disturbances in this transition region is speedy at the  $0^\circ$  angle of attack, and the head of this transition region has no identifiable regular vortices similar to the head of the region on the leeward side. In addition, the streamwise vortex instability region of the windward vortex region and the cross-flow instability region of the windward cross-flow region with a small vortex structure below are connected at their tail. Moreover, as shown in the red box in Fig. 30, it is noteworthy that there are multiple disturbances outside the transition region. These disturbances gradually develop toward the inside of the transition region, roughening the boundary of the transition region, which is consistent with the observation in Fig. 29(a).

As the vortex structure is shown in Fig. 31, the development of the disturbance at  $7^\circ$  angle of attack is significantly slower than that at  $0^\circ$  angle of attack. Initially, the disturbance at the head of the transition shows as a wide flattened crescent-shaped vortex. With the development of the disturbance, the crescent-shaped vortex is stretched backward and connected to the crescent-shaped vortex in the opposite direction below, forming a ring-shaped vortex, before eventually losing stability and transition occurs. In addition, a new streamwise direction vortex is generated in the transition region indicated by the black dotted line in Fig. 29(d). The transition type of the streamwise vortex is consistent with that of the original transition region.

The streamline's distribution can help to provide insights into the flow patterns in the transition region and understand the causes of the transition mechanism. As shown in Fig. 32, at  $0^\circ$  angle of attack, the flows from the head of the centerline of the windward side and the attachment line of the shoulder converge in the windward vortex region, which results in the transition occurring. The flow inside the transition region is stronger, while outside, it is weaker. As a result,

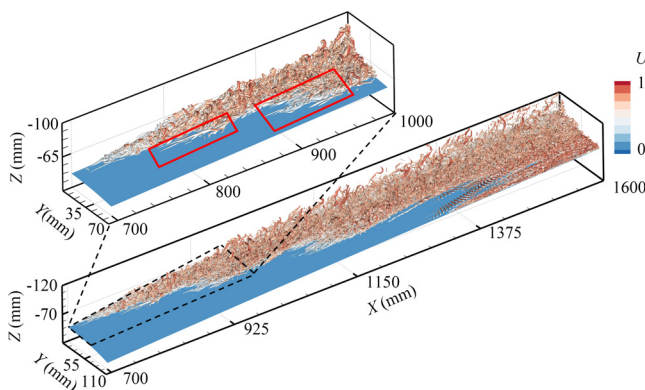


FIG. 30. Instantaneous flow pattern of the windward vortex region at  $0^\circ$  angle of attack (same settings as Fig. 19).

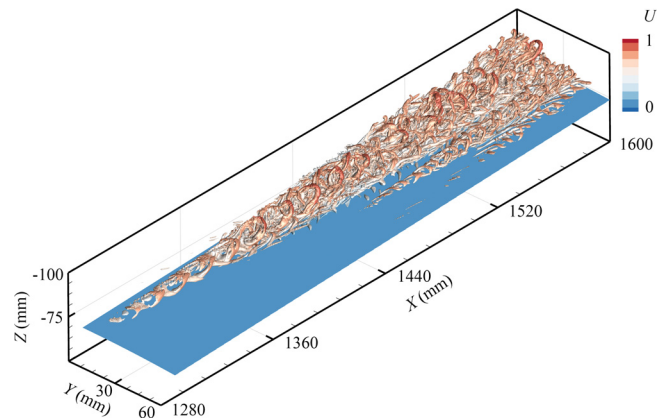


FIG. 31. Instantaneous flow pattern of the windward vortex region at  $7^\circ$  angle of attack (same settings as Fig. 19).

the flow outside the transition region changes direction at the transition region's boundary and converges with the flow in the original direction. As shown in the red box in Fig. 32, it is shown that the flows converge in the areas outside the transition region. As the angle of attack increases, the flow in the head region of the centerline of the windward side is enhanced and its range expands, while the flow from the shoulder attachment line to the windward centerline is weakened and its range decreases. As shown in the lower part of Fig. 32, the entire windward vortex region at  $7^\circ$  angle of attack is only located within the range of flow from the head area of the windward side centerline. The transition mechanism has changed compared to that at  $3^\circ$  angle of attack and the transitions will not occur beyond the boundary of the transition region. As a result, the boundary of the transition region becomes smooth. In addition, the transition in the region at  $7^\circ$  angle of attack is caused by the flow gradually becoming increasingly unstable along the streamline.

### F. Windward cross-flow region

As shown in Fig. 15, with the angle of attack increasing, the range of the windward cross-flow region obviously decreases, while the distinct transition spot not even be observed at  $5^\circ$  and  $7^\circ$  angles of attack.

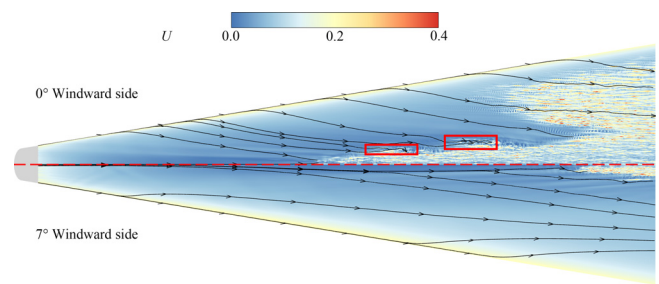


FIG. 32. Instantaneous streamwise velocity distribution of the windward side at different angles of attack, depicted by a wall-normal slice (at the 10th grid point from the wall): Take the centerline of the model as the boundary. The upper part of the figure is the simulation at  $0^\circ$  angle of attack, and the lower part is the simulation at  $7^\circ$  angle of attack.

**TABLE IX.** Transition region data of the windward cross-flow region at different angles of attack.

Angle of attack (°)	$C_{fmax}$ ( $\times 10^{-2}$ )	$X_{head}$ (mm)	$Y_{t_i}$ (mm)	$Y_{t_o}$ (mm)	$Y_w$ (mm)
0	0.1926	1212.93	79.77	266.11	186.34
3	0.2233	1268.02	87.80	259.62	171.82
5	...	...	...	...	...
7	...	...	...	...	...

The definition of the windward cross-flow region is similar to that of the other three transition regions (seen from Sec. III C). Since the transition region cannot be determined at 5° and 7° angle of attack, only the data of the transition region at 0° and 3° angle of attack are obtained. The specific transition region data are shown in Table IX (the definitions of parameters are the same as that in Table VI). It can be obvious that, the transition location ( $X_{head}$ ) at 3° angle of attack moves backward compared to that at the 0° angle of attack. Moreover, both sides of the tail of the transition region ( $Y_{t_i}$  and  $Y_{t_o}$ ) move toward the inside of the transition region at 3° angle of attack, resulting in a narrowing of the width of the transition region.

As illustrated in Figs. 33(a) and 33(b), the windward cross-flow region exhibits a triangular shape at 0° and 3° angle of attack. The region is surrounded by longitudinal bands (along the streamwise direction). Previous studies<sup>37,42</sup> have confirmed that these longitudinal bands are associated with cross-flow waves. In addition, some transversal bands are equally spaced within these longitudinal bands. These transversal bands are believed to develop from secondary instabilities of the cross-flow waves. Moreover, by comparing Fig. 33 with the

time-averaged skin friction coefficient distribution in Fig. 15, it is observed that no obvious bands are present, suggesting that these bands arise from traveling cross-flow waves. As shown in Figs. 33(c) and 33(d), the windward cross-flow region has hardly been observed at 5° and 7° angles of attack. Among them, only minor longitudinal bands can be observed outside the model’s tail at 5° angle of attack, while these longitudinal bands disappear at 7°.

Figures 34 and 35 show the vortex structure of the windward cross-flow region at 0° and 7° angle of attack, respectively. Observing the vortex structure at 0° angle of attack in Fig. 34, it can be clearly seen that there are many longitudinally distributed oblique rolls around the transition region, which consistent with the positions of the corresponding longitudinal bands in Fig. 33(a). The upper parts of these oblique rolls are connected, resulting in a striped vortex with a uniform azimuth angle. However, as shown in Fig. 35, the amount and distribution of oblique rolls are significantly reduced at 7° angle of attack and no transition occurs.

According to the streamline’s distribution of the windward side in Fig. 32, it can be found that the windward cross-flow region is generated by the cross-flow instability originating from the shoulder attachment line region. In addition, the cross-flow around the windward cross-flow region is strong and ranges wide range at 0° angle of attack. As the angle of attack increases, the flow from the head of the model is gradually strengthened and expands toward the shoulder attachment line region. However, the cross-flow above the region of the attachment line of the shoulder is further weakened, narrowing the flow range to the small region above the attachment line of the shoulder. As a result, the range of the windward cross-flow region gradually decreases as the angle of attack increases. Moreover, the windward cross-flow region further narrows or even disappears due to the weakening cross-flow on the windward side.

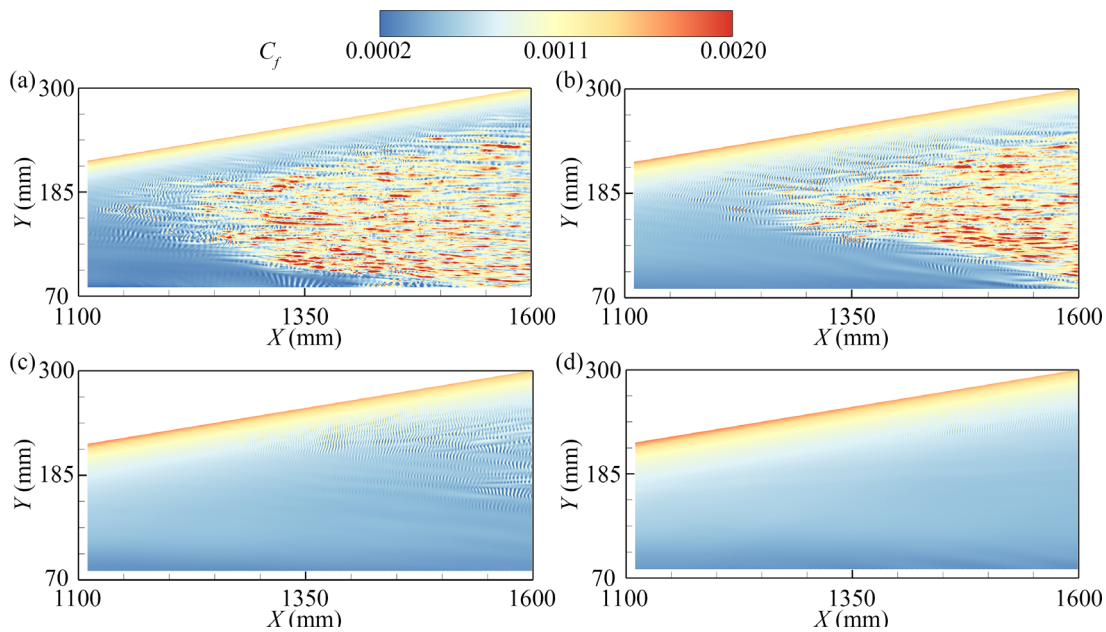


**FIG. 33.** Instantaneous skin friction coefficient distribution of the windward cross-flow region at different angles of attack: (a) 0°, (b) 3°, (c) 5°, and (d) 7°.

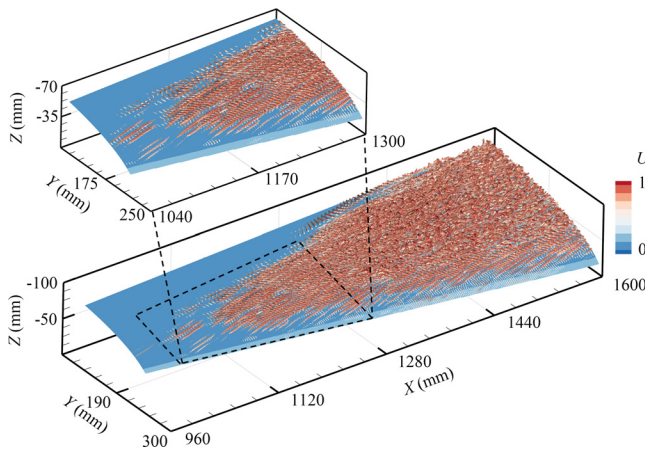


**FIG. 34.** Instantaneous flow pattern of the windward cross-flow region at 0° angle of attack (same settings as Fig. 19).

**IV. SUMMARY AND CONCLUSIONS**

This paper performs direct numerical simulations (DNS) of hypersonic boundary layer transition over a Hypersonic Transition Research Vehicle (HyTRV) model lifting body under a typical Mach 6 hypersonic wind tunnel flow condition. Transitions are simulated at four angles of attack: 0°, 3°, 5°, and 7°. Random blowing and suction perturbations are introduced to trigger the transition. The results of the DNS data show that transition occurs in four regions of the HyTRV model: the shoulder cross-flow and vortex region, the shoulder vortex region, the windward vortex region, and the windward cross-flow region. Summary and conclusions are drawn for each region as follows:

For the shoulder cross-flow and vortex region, as the angle of attack increases, the transition location moves forward and the transition range expands. At large angles of attack (5° and 7°), the development of the streamwise vortex at the tail of the model leads to the division of the triangular transition region into three parts: the cross-flow instability region on both sides and the streamwise vortex instability region sandwiched in the middle. The presence of the streamwise vortex leads to a significant increase in cross-flow instability in the

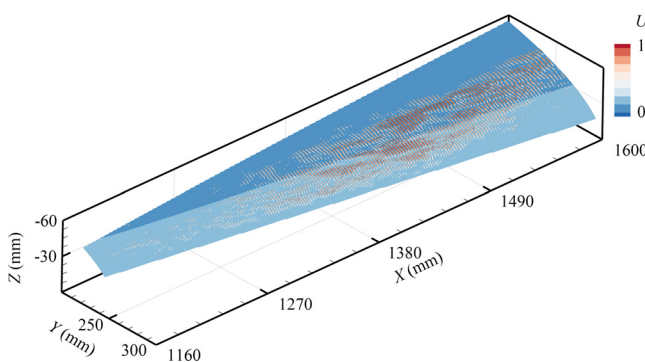


**FIG. 35.** Instantaneous flow pattern of the windward cross-flow region at 7° angle of attack (same settings as Fig. 19).

upper region of the transition region. It also leads to the generation of a region with a high skin friction coefficient in front of the transition region.

For the shoulder vortex region, as the angle of attack increases, the transition range expands, and the transition region moves toward the centerline of the leeward side. The transition location moves forward at small angles of attack (0° and 3°). However, at large angles of attack, two disturbance modes appear at the transition region’s head due to the flow separation of the model’s head. At 5° attack angle, the transition location moves backward owing to the delay in flow convergence. While at 7° attack angle, since the transition regions on both sides of the model gradually merge during the movement, the transition location moves forward again. Furthermore, the enhancement of the cross-flow around the shoulder cross-flow and vortex region may generate a new streamwise vortex instability region between the two transition regions on the leeward side.

For the windward vortex region, as the angle of attack increases, the transition location moves backward and the transition range decreases. At small angles of attack, the strong flow in the transition region may cause the flow direction outside the transition region to change significantly at the transition boundary. It results in the boundary of the transition region becoming rough due to the occurrence of the other transitions. At large angles of attack, the flow near the centerline of the windward side is enhanced and the flow range expands, which directly leads to a change in the transition mechanism, thus the boundary of the transition region becomes smooth.

For the windward cross-flow region, the triangular transition region is surrounded by longitudinally distributed oblique rolls from traveling cross-flow waves at small angles of attack. As the angle of attack increases, the intensity and the range of the cross-flow on the windward side both decreases. As a result, the transition location moves backward, and the transition range tends to become narrow, then transition region ultimately disappears.

Based on the analysis results of the HyTRV model lifting body at different angles of attack in this paper, the shoulder cross-flow and vortex region and shoulder vortex region on the leeward side exhibit more complex transitional behaviors than the transition regions on the windward side under the interaction of streamwise vortex instability and cross-flow instability. However, the transition mechanism of these complex transitional behaviors and their impact need to study further. Hence, in the follow-up experimental verification and research, it is recommended to focus on the transitional behaviors of the two transition regions on the leeward side.

**ACKNOWLEDGMENTS**

This work was supported by the National Key Research and Development Program of China (No. 2019YFA0405300) and NSFC Projects (Nos. 12232018, 12072349, and 12202457).

The authors thank the National Supercomputer Center in Tianjin (NSCC-TJ) and the National Supercomputer Center in Guangzhou (NSCC-GZ) for providing computer time.

**AUTHOR DECLARATIONS**

**Conflict of Interest**

The authors have no conflicts to disclose.

## Author Contributions

**Hongyuan Men:** Conceptualization (equal); Data curation (equal); Formal analysis (equal); Methodology (equal); Software (equal); Validation (equal); Writing – original draft (equal); Writing – review & editing (equal). **Xinliang Li:** Funding acquisition (equal); Investigation (equal); Project administration (equal); Software (equal); Validation (equal); Writing – review & editing (equal). **Hongwei Liu:** Funding acquisition (equal); Investigation (equal); Project administration (equal); Software (equal); Validation (equal); Writing – review & editing (equal).

## DATA AVAILABILITY

The data that support the findings of this study are available from the corresponding author upon reasonable request.

## REFERENCES

- <sup>1</sup>H. Yang, H. Liang, S. Guo *et al.*, “Research progress of hypersonic boundary layer transition control experiments,” *Adv. Aerodyn.* **4**(1), 1–54 (2022).
- <sup>2</sup>Y. Duan, S. Yao, S. Li, and P. Yu, “Review of progress in some issues and engineering application of hypersonic boundary layer transition,” *Acta Aerodyn. Sin.* **38**(2), 391–403 (2020).
- <sup>3</sup>J. Chen, X. Yuan, G. Tu *et al.*, “Recent progresses on hypersonic boundary-layer transition,” *Sci. Sin-Phys. Mech. Astron.* **49**(11), 114701–114134 (2019).
- <sup>4</sup>G. Tu, J. Chen, X. Yuan *et al.*, “Progress in flight tests of hypersonic boundary layer transition,” *Acta Mech. Sin.* **37**(11), 1589–1609 (2021).
- <sup>5</sup>G. Gao, Q. Li, N. Chen, and Y. Song, “The influence of asymmetric transition on stability of hypersonic aircrafts,” *Tactical Missile Technol.* **6**, 12–15 (2012).
- <sup>6</sup>J. Chen, G. Tu, Y. Zhang, G. Xu, X. Yang, and C. Chen, “Hypersonic boundary layer transition: What we know, where shall we go,” *Acta Aerodyn. Sin.* **35**(3), 311–337 (2017).
- <sup>7</sup>J. S. Luo, “Transition and prediction for hypersonic boundary layers,” *Acta Aeronaut. Astronaut. Sin.* **36**(1), 357–372 (2015).
- <sup>8</sup>H. Nie, W. Song, Z. Han *et al.*, “A surrogate-based eN method for compressible boundary-layer transition prediction,” *J. Aircr.* **59**(1), 89–102 (2022).
- <sup>9</sup>S. Dong, F. Tong, M. Yu *et al.*, “Effects of wall temperature on two-point statistics of the fluctuating wall shear stress and heat flux in supersonic turbulent boundary layers,” *Phys. Fluids* **34**(6), 065114 (2022).
- <sup>10</sup>Q. Liu, G. Tu, and Z. Luo, “Progress in hypersonic boundary layer transition delay control,” *Acta Aeronaut. Astronaut. Sin.* **43**(7), 25357–025357 (2022).
- <sup>11</sup>X. Yuan, F. Tong, W. Li *et al.*, “Wall-attached temperature structures in supersonic turbulent boundary layers,” *Phys. Fluids* **34**(11), 115116 (2022).
- <sup>12</sup>J. J. Bertin and R. M. Cummings, “Fifty years of hypersonics: Where we’ve been, where we’re going,” *Prog. Aerosp. Sci.* **39**(6–7), 511–536 (2003).
- <sup>13</sup>Z. Heng and Z. Hanxin, “Two problems in the transition and turbulence for near space hypersonic flying vehicles,” *Acta Aerodyn. Sin.* **35**(2), 151–155 (2017).
- <sup>14</sup>M. Gaster and I. Grant, “An experimental investigation of the formation and development of a wave packet in a laminar boundary layer,” *Proc. R. Soc. London A* **347**(1649), 253–269 (1975).
- <sup>15</sup>Y. Zhang, J. Chen, X. Yuan *et al.*, “Hypersonic boundary layer receptivity on flat plate with blunt leading edge due to acoustic disturbance,” *J. Phys.: Conf. Ser.* **1786**(1), 012037 (2021).
- <sup>16</sup>V. I. Borodulin, V. R. Gaponenko, Y. S. Kachanov *et al.*, “Late-stage transitional boundary-layer structures. Direct numerical simulation and experiment,” *Theor. Comput. Fluid Dyn.* **15**, 317–337 (2002).
- <sup>17</sup>V. I. Kornilov, “Transition of the boundary layer on a flat plate at supersonic and hypersonic velocities,” *Thermophys. Aeromech.* **16**(3), 347–354 (2009).
- <sup>18</sup>A. Fedorov, “Transition and stability of high-speed boundary layers,” *Annu. Rev. Fluid Mech.* **43**, 79–95 (2011).
- <sup>19</sup>X. Lu, S. Yi, L. He, X. Liu, and H. Niu, “Experimental investigation of the hypersonic boundary layer transition on a 45° swept flat plate,” *Fluid Dyn.* **55**(1), 111–120 (2020).
- <sup>20</sup>X. Chen, J. Chen, and X. Yuan, “Hypersonic boundary layer transition on a concave wall induced by low-frequency blowing and suction,” *Phys. Fluids* **34**(11), 114105 (2022).
- <sup>21</sup>J. Chen, S. Dong, X. Chen *et al.*, “Stationary cross-flow breakdown in a high-speed swept-wing boundary layer,” *Phys. Fluids* **33**(2), 024108 (2021).
- <sup>22</sup>P. Paredes, B. Venkatachari, M. M. Choudhari *et al.*, “Toward a practical method for hypersonic transition prediction based on stability correlations,” *AIAA J.* **58**(10), 4475–4484 (2020).
- <sup>23</sup>X. Xu, S. Yi, F. Zhang *et al.*, “Influences of steps on the hypersonic boundary-layer transition on a cone,” *AIAA J.* **59**(2), 439–446 (2021).
- <sup>24</sup>K. F. Stetson and R. Kimmel, “On the breakdown of a hypersonic laminar boundary layer,” AIAA Paper No. 93-896, 1993.
- <sup>25</sup>C. Su and H. Zhou, “Transition prediction of a hypersonic boundary layer over a cone at small angle of attack—with the improvement of eN method,” *Sci. China Ser. G* **52**, 115–123 (2009).
- <sup>26</sup>X. Li, D. Fu, and Y. Ma, “Direct numerical simulation of hypersonic boundary layer transition over a blunt cone with a small angle of attack,” *Phys. Fluids* **22**(2), 025105 (2010).
- <sup>27</sup>Q. Wang, X. Xiang, S. Dong *et al.*, “Wall temperature effects on the hypersonic boundary-layer transition over an inclined, blunt cone,” *Phys. Fluids* **35**, 024107 (2023).
- <sup>28</sup>H. Zhu, G. Wang, Q. Sun, and J. Fan, “Numerical evaluation on aerodynamics of typical hypersonic configurations for hypersonic flight,” *Acta Aerodyn. Sin.* **30**(3), 365–372 (2012).
- <sup>29</sup>F. Wang, Y. Shen, W. Yao *et al.*, “Aerodynamic and aerothermal numerical simulation of hypersonic lifting body configuration,” *Acta Aerodyn. Sin.* **19**(4), 439–445 (2001).
- <sup>30</sup>H. Tian, Y. Ye, Q. Jiang, and X. He, “Investigation of real gas effects on local flow separation of lifting body rudder,” *Acta Aerodyn. Sin.* **33**(3), 330–337 (2015).
- <sup>31</sup>S. L. Chernyshev, S. V. Lyapunov, and A. V. Wolkov, “Modern problems of aircraft aerodynamics,” *Adv. Aerodyn.* **1**(1), 1–15 (2019).
- <sup>32</sup>Q. Gao, J. Li, and Q. Li, “Study on lateral stability of hypersonic lifting-configurations,” *J. Exp. Fluid Mech.* **29**(1), 43–48 (2015).
- <sup>33</sup>V. Wartemann, H. Weihs, and T. Eggers, “Comparison of faceted and blunt lifting bodies for reentry flights,” *J. Spacecr. Rockets* **55**(4), 877–886 (2018).
- <sup>34</sup>S. Liu, X. Yuan, Z. Liu, Q. Yang, G. Tu, X. Chen, Y. Gui, and J. Chen, “Design and transition characteristics of a standard model for hypersonic boundary layer transition research,” *Acta Mech. Sin.* **37**(11), 1637–1647 (2021).
- <sup>35</sup>J. Chen, G. Tu, B. Wan, X. Yang, Q. Yang, Y. Zhuang, and X. Yang, “Characteristics of flow field and boundary-layer stability of HyTRV,” *Acta Aeronaut. Astronaut. Sin.* **42**(6), 264–279 (2021).
- <sup>36</sup>H. Qi, X. Li, C. Yu, and F. Tong, “Direct numerical simulation of hypersonic boundary layer transition over a lifting-body model HyTRV,” *Adv. Aerodyn.* **3**(1), 1–21 (2021).
- <sup>37</sup>X. Chen, S. Dong, G. Tu, X. Yuan, and J. Chen, “Boundary layer transition and linear modal instabilities of hypersonic flow over a lifting body,” *J. Fluid Mech.* **938**, A8 (2022).
- <sup>38</sup>G. Dang, S. Liu, T. Guo, J. Duan, and X. Li, “Direct numerical simulation of compressible turbulence accelerated by graphics processing unit: An open-source high accuracy accelerated computational fluid dynamic software,” *Phys. Fluids* **34**(12), 126106 (2022).
- <sup>39</sup>X. Li, Y. Leng, and Z. He, “Optimized sixth-order monotonicity-preserving scheme by nonlinear spectral analysis,” *Int. J. Numer. Methods Fluids* **73**(6), 560–577 (2013).
- <sup>40</sup>C. Bogey, N. D. Cacqueray, and C. Bailly, “A shock-capturing methodology based on adaptative spatial filtering for high-order non-linear computations,” *J. Comput. Phys.* **228**(5), 1447–1465 (2009).
- <sup>41</sup>J. C. R. Hunt, A. A. Wray, and P. Moin, “Eddies, streams, and convergence zones in turbulent flows,” in *Proceedings of the 1988 Summer Program, Center for Turbulence Research* (Stanford, 1988), pp. 193–208.
- <sup>42</sup>M. W. Tufts, M. P. Borg, N. J. Bisek, and R. L. Kimmel, “High-fidelity simulation of HIFiRE-5 boundary-layer transition,” *AIAA J.* **60**(4), 2039–2050 (2022).